ELSEVIER

Nuclear Engineering and Design 155 (1995) 115–157

Nuclear Engineering and Design

Premixing-related behavior of steam explosions

S. Angelini[a,b], W.W. Yuen[a,b], T.G. Theofanous[a]

[a]*Center for Risk Studies and Safety, Department of Chemical and Nuclear Engineering, University of California, Santa Barbara, CA 93106, USA*

[b]*Department of Mechanical and Environmental Engineering, University of California, Santa Barbara, CA 93106, USA*

Abstract

Three recently published premixing experiments, the MAGICO, MIXA, and FARO, are discussed comparatively, and two of them, the MAGICO and FARO, are analyzed with the help of the computer code PM-ALPHA. The results of these analyses are shown to provide quantitative interpretations of the data, and to suggest conditions/measurements in further experiments to enhance the insights thus obtained. Also, a quantitative radiography technique is described and applied to MAGICO for the measurement of chordal-averaged void fractions in the mixing zone. The results are in excellent agreement with PM-ALPHA predictions, thus confirming the previously reported good comparisons with the local (point) measurements of FLUTE.

1. Introduction

Premixing is the multiphase transient obtained during the pouring of a high temperature melt in a liquid coolant; given an appropriate trigger, this transient can be transformed into an explosion (commonly referred to as a "steam explosion"; such explosions can occur with a variety of "hot"/"cold" liquid pairs, but without loss of generality we will speak here of a "melt" and "water"). An explosion can be triggered at any time by an externally supplied pressure pulse, or it can occur spontaneously as a result of a local thermal interaction if conditions for such are obtained during the premixing. In any case, the premixing transient provides the initial conditions for the explosion (or so-called "escalation" and "propagation" phases) and as such it provides the basis for assessing "what constitutes an adequate trigger, and the "magnitude of the energetics obtained from a resulting explosion". In general, these initial conditions can be characterized by the space–time variations of the volume fractions of the three constituents (melt, water, and steam); however, of particular significance is the so-called "water depletion" phenomenon.

The water depletion phenomenon refers to the formation of a high void (steam) fraction region in the major central portion of large-scale melt pours in water. This "steam bubble" is due to the high heat transfer rates and associated steaming that "drive" the water out while at the same time it is being vaporized. This means that large quantities of melt cannot coexist with large quantities of water in a coarsely mixed configuration, i.e. in a condition that is conducive to an efficient thermal interaction.

On the one hand such largely voided premixtures are not easily susceptible to triggering, and

Elsevier Science S.A.
SSDI 0029-5493(94)00873-W

on the other hand, even assuming that an explosion can develop, it would be very inefficient. This allows for putting bounding limits on interacting masses from arbitrarily large pours, and thus it has served as a central element of the argument against the α-mode containment failure in the past (Steam Explosions Review Group, 1985; Theofanous, 1987). This is important because then, and this remains true now, late-phase, core-melt progression uncertainties do not allow a rigorous argument to be made against massive molten corium dumps into the lower plenum.

The water depletion phenomenon was first conjectured by Henry and Fauske (1981), and Bankoff and Han (1984) made an attempt to compute it. A first actual quantification was offered by Abolfadl and Theofanous (1987), using a two-fluid model, and this was further refined by a three-fluid formulation and the PM-ALPHA code (Amarasooriya, 1991). An independent but similar three-fluid formulation also has been pursued under the CHYMES code development effort in the UK (Fletcher, 1991), and the first comparisons with the above-mentioned PM-ALPHA results have just been published (Fletcher, 1992). Except for not accounting for subcooling, these CHYMES results can be interpreted to be supportive to PM-ALPHA and the predicted water depletion phenomenon (Theofanous, 1993). The first experimental verification of this phenomenon was made in the MAGICO experiment a little more than 1 year ago (Theofanous, 1991) and a detailed presentation of the first two series of experiments together with PM-ALPHA predictions was given in the recent NURETH-5 meeting (Angelini, 1992). The initial data from another premixing experiment the MIXA, tied to the CHYMES verification effort, were also presented in the same meeting (Denham, 1992) and the first data from the FARO experiment at the CRC, Ispra have just become available (Magallon, 1992, 1993). Clearly, the major new developments in this area will occur as these and subsequent data are studied and interpreted with the help of these codes. The main purpose of this paper is to discuss these experiments from such a standpoint and to take some initial, illustrative, steps in this direction.

2. Overview of the premixing experiments

As noted above, there are three premixing experiments that are currently active (a fourth one is planned in Grenoble, France). Of these, the MAGICO and MIXA are specifically designed for this purpose. The stated scope of FARO is not specific to premixing; however, it provides an interesting complement from this standpoint, also, to the MAGICO and MIXA experiments. Indeed, viewed as a group, these three experiments provide a nice sequence from the well-defined conditions of MAGICO (fixed particle sizes), to MIXA (prefragmented melt pours into more-or-less regular streams, and apparent capability to observe particle sizes in flight), to the rather poorly defined melt conditions entering the water and no possibility of direct observation of the ensuing interaction in FARO. Except perhaps for the relatively small (compared to reactor) quantities of melt, the FARO is quite prototypic, and very valuable for this reason, to its main purpose: to determine the extent of quenching possible in the lower plenum at high pressures, and the extent, if any, of thermal attack on the lower head. As usual, gaining in prototypicality creates loss of definition, both in initial/boundary conditions, as well as in observations/measurements that characterize the interaction, and this loss is quite detrimental in achieving the basic understanding necessary for analyses to be useful in predicting the behavior in reactor accidents. On the other hand, one would be amiss expecting to securely bridge the gap between the well-defined experiments and the reactor without the actual experience of dealing with the less well-defined but more prototypical tests. We believe that it is very fortunate that these three independently developed programs are so congruent to the overall purpose.

The major aspect of this view is that MAGICO is suitable for the unambiguous testing of the three-fluid formulation, especially of the phase-change and momentum interaction parts, while the MIXA and FARO can provide important perspectives on the extent and rate of melt breakup under two different melt-entry conditions. All tests involve the pouring of a hot mass (in liquid or solid particle form) into a liquid pool, but in addition

to the above, there are other interesting differences well-suited to the overall task of understanding premixing in all its major aspects. A brief account of these other aspects is given below.

Regarding measurements, the MAGICO is focused on local steam volume fractions, as this is the key variable characterizing a premixture from the explosivity/energetics point of view (Theofanous, 1993; Yuen, 1993). This is a very difficult measurement, but it became possible using FLUTE (Angelini, 1992) and X-rays (later in this paper). In MIXA, on the other hand, an integral measure of the thermal interaction is obtained by measuring the steam flow rates during the transient and observing the overall level swell in the interaction vessel. In both these experiments, the interaction progresses essentially at atmospheric pressure (i.e. there is no feedback from steaming). The same approach of measuring the steam generation rate is also intended for FARO; however, the two tests reported so far were performed with a closed interaction vessel which, as explained later in this paper, provides analysis-testing opportunities not previously anticipated nor available so far from the other two tests. Briefly, with a closed vessel, the thermal interaction leads to pressurization and an interesting boiling feedback due to the induced rise in saturation temperature. In these tests, this feedback was further accentuated by radiation heat transfer to the steam in the cover gas space. In addition, FARO is run at high pressures (~ 5 MPa), which provides opportunities (but also complications) for testing integral predictions in that constitutive laws are not as well known at elevated pressures (i.e. film boiling from spheres in subcooled water and high pressures). Regarding other measurements in both MAGICO and MIXA, the interactions have been observed visually (by high-speed photography), which makes possible melt-front and two-phase zone tracing, and perhaps even particle size measurements in MIXA (the extent to which this can provide the full information needed is yet to be determined). In FARO, no such data are possible, but some rough idea of melt-front advancement and level swell seems to be possible to extract from thermocouple signals.

Regarding melt temperature and delivery conditions, there are some interesting differences to be noted. In MIXA, the melt is heated up to ~ 3600 K. At such high temperatures, the optical depth of the emitted radiation in water increases rapidly so that non-local deposition of radiant energy becomes very important. For realistic simulations, one must treat the mixing zone as an absorbing-emitting medium taking into account spatial variations in melt and liquid volume fractions, and one must even include, in the scale of MIXA, the surrounding liquid zone, if any, and the container boundaries. For the FARO test (melt at 2650 °C) and the reactor case, on the other hand, such effects are negligible. We are currently modifying PM-ALPHA for this specialized heat transfer regime of MIXA, and for this reason, no comparisons are available at this time. Turning to melt delivery, in MIXA the pour is prefragmented (by passing it over a grid made of graphite bars) and characterized (length scales, velocities, and volume fraction) from high-speed movies; in FARO, the melt is allowed to pour by gravity through a 10-cm nozzle and to contact water after a fall of ~ 2 m through the cover gas (steam and argon) space. Melt delivery times are estimated, presumably by thermocouple data, but at this stage, it is not clear how this is done, nor what are the uncertainties involved.

3. Overview and organization of this paper

As noted already, the main purpose of this paper is to study the results from the MAGICO and FARO experiments with the help of PM-ALPHA. There is also an experimental component in addressing the local void fractions in MAGICO by an X-ray diagnostic technique, as an independent check on the FLUTE data reported earlier. To preserve some cohesiveness of presentation, this independent, experimental component is relegated to the appendix.

In the discussion of the experiments, we assume that the reader is already familiar with the original papers on them, i.e. Angelini et al. (1992) for MAGICO, and Magallon and Hohmann (1993) for FARO. Our presentation begins, in each case, with

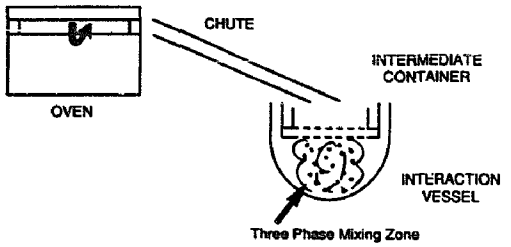

Fig. 1. Schematic of the MAGICO experiment.

the aspects relevant to the simulations and how they were effected, and in the main part focuses on the comparisons and related interpretations. For completeness, we also provide a recently implemented numerically advantageous treatment of phase-change in PM-ALPHA. (The complete formulation is also included, for convenience, in the appendix.) Starting from this introductory PM-ALPHA topic, the presentation proceeds from MAGICO to FARO.

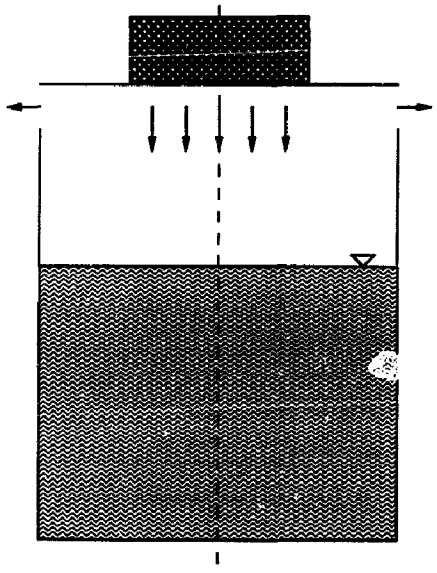

Fig. 2. Illustration of the flow field utilized in PM-ALPHA for the interpretation of the MAGICO experiment.

4. The PM-ALPHA code

In the original formulation, the rate of phase change (J) was calculated such as to maintain the liquid phase saturated at the local pressure. This was accomplished by specifying ($J > 0$ for vaporization)

$$J = \frac{\rho'_g}{\tau_c}\left\{\left(\frac{p_s}{p}\right)^{1/\gamma} - 1\right\} \qquad (1)$$

where γ is the usual specific heat ratio, p_s is the saturation pressure of liquid temperature, and p is the actual local pressure. The parameter τ_c is a relaxation time for thermodynamic equilibrium, and this model could couple very nicely with the iteration process given the correct amount of phase change accounting, implicitly, for pressure changes. We found it convenient to choose this relaxation time equal to the time step, but the results are not sensitive at least up to 5 times as large. With this model PM-ALPHA could accommodate a subcooled liquid, but numerically in a somewhat cumbersome way. On the other hand, the above formulation has occasionally caused criticism because of its heuristic nature. To eliminate this nuisance and at the same time achieve an explicit treatment of phase change, as a rate process, i.e. reflecting non-negligible amounts of superheat as well as subcooling, we replace Eq. (1) with

$$J = \frac{1}{h_g - h_l}[R_g(T_g - T_s) + R_l(T_l - T'_s)] \qquad (2)$$

When the liquid and vapor are at their thermodynamically stable states (i.e. saturated or subcooled liquid, saturated or superheated vapor), the transfer coefficients (R_g and R_l) are evaluated based on a set of constitutive laws that are consistent with the flow regime approach used previously. When the two phases are predicted to be in thermodynamically unstable states (i.e. superheated liquid and subcooled vapor), R_l and R_g are adjusted upward to recover thermodynamic equilibrium. Sample calculations carried out with Eq. (2) and this approach are in excellent agreement with the previous results (i.e. based on Eq. (1)). For convenience, the complete model after this modification is given in Appendix A.

5. Consideration of the MAGICO experiment

5.1. Simulation aspects

The basic concept of the experiment is illustrated in Fig. 1. Tens-of-kilograms quantities of mm-sized steel balls are heated to a uniform temperature (up to 1000 °C), then transferred to an intermediate container equipped with a dumping mechanism, and within a few seconds are released into a pool of saturated (atmospheric pressure) water. The pool cross section is rectangular, 40.5 cm on the side. The major experimental parameters are pool depth (15, 25 and 50 cm), particle size (1.5 and 2.4 mm), particle temperature (600–1000 °C), pour diameter (12 and 20 cm), and particle entry velocity (corresponding to free fall from 5, 15, and 25 cm, with an initial velocity of 0.72 m s^{-1}). The initial velocity was obtained from high-speed movies and found to be independent of particle size or the particle depth in the intermediate container. From this and the measured total mass pour rate, the particle volume fraction at the outlet of the intermediate container could also be obtained as 1.87 and 2.5% for the 2.4 and 1.5 mm particles, respectively. Temperature losses in the intermediate container were minor, and the actual temperature of the particulate just before being released was reported.

Thus, for any particular experiment, all conditions necessary for the simulation are exactly specified, and only one minor approximation and one minor non-ideality need to be mentioned. The approximation involves representing the rectangular cross section of the pool by a circular one of diameter equal to the side of the rectangular tank. The pour area is also circular, and this allows the simulations to be performed in axisymmetric cylindrical geometry. The non-ideality involves the presence of a few cold balls in the front of the falling particle cloud. These are the balls that fill the holes in the 6-mm thick plate of the dumping mechanism; they are cold because of heat losses to the plate, and they fall in a "formation" with a considerably larger particle volume fraction than the rest of the cloud (this was confirmed experimentally). Certainly, these balls cannot influence the interaction itself, but one needs to be aware of them for some timing details and especially for interpreting the very initial FLUTE signal as previously discussed (Angelini, 1992).

The actual flow field employed in PM-ALPHA is illustrated in Fig. 2. All geometric features and inlet conditions are specified for each experiment, as discussed above, except for the vent openings. Since in the experiment the pool top was completely open to the atmosphere, the only requirement is that these vent openings are chosen of large enough area to avoid any pressurization in the vapor space. Cell sizes are 2.0 cm in the radial direction and 2.5 cm in the axial direction, which gives 10 radial cells and 12–26 axial cells, depending on tank depth and free-fall region. Node size studies showed that this is adequate.

The experimental data consist of mixing-zone-average void fractions obtained from high-speed movies (from the level rise around the mixing zone), and local void-fraction transients using a new instrument, the FLUTE. Both of these quantities can be easily obtained from the results of the PM-ALPHA computations for comparison with the data, and such comparisons have been reported previously (Angelini, 1992; Theofanous, 1992) with very good agreement. Also, chordal-average steam volume fractions can be obtained for comparisons with the projection-type information obtained from X-ray radiography, as described in Appendix B. These comparisons are also very good. As a next step in this study of MAGICO, we examine some of the more detailed features of the interactions as revealed in the computations and relate them, when possible, to the structure of the mixing zone as seen by direct visualization.

5.2. The detailed structure of interactions in MAGICO

The premixing transient is a vastly complicated process, which besides the primary quantity of interest, the space–time evolution of the void fraction, has a number of other interesting features. These features relate to the detailed motions and associated interactions, and they are significant in creating the conditions within which the void fraction pattern develop. We study these motions here in terms of the calculated steam and

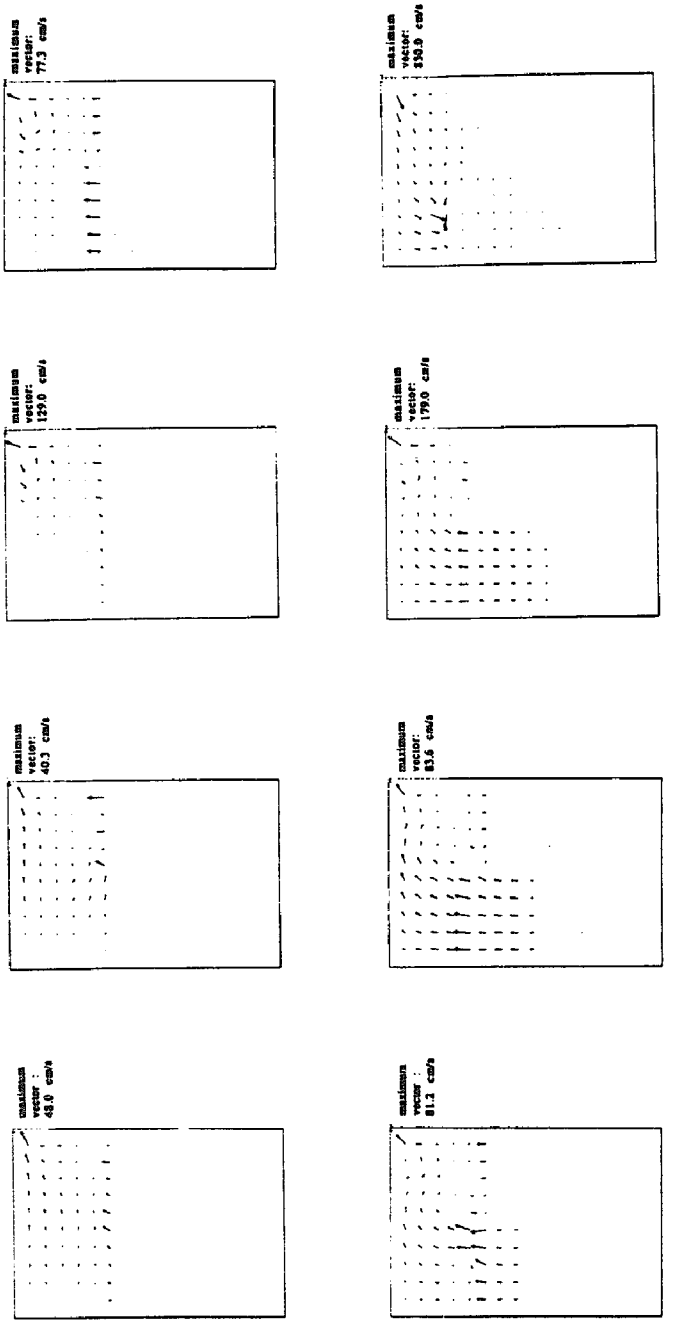
maximum vector: 77.3 cm/s
maximum vector: 350.9 cm/s
maximum vector: 129.0 cm/s
maximum vector: 179.0 cm/s
maximum vector: 40.3 cm/s
maximum vector: 83.6 cm/s
maximum vector: 45.0 cm/s
maximum vector: 81.2 cm/s

Fig. 3(a)

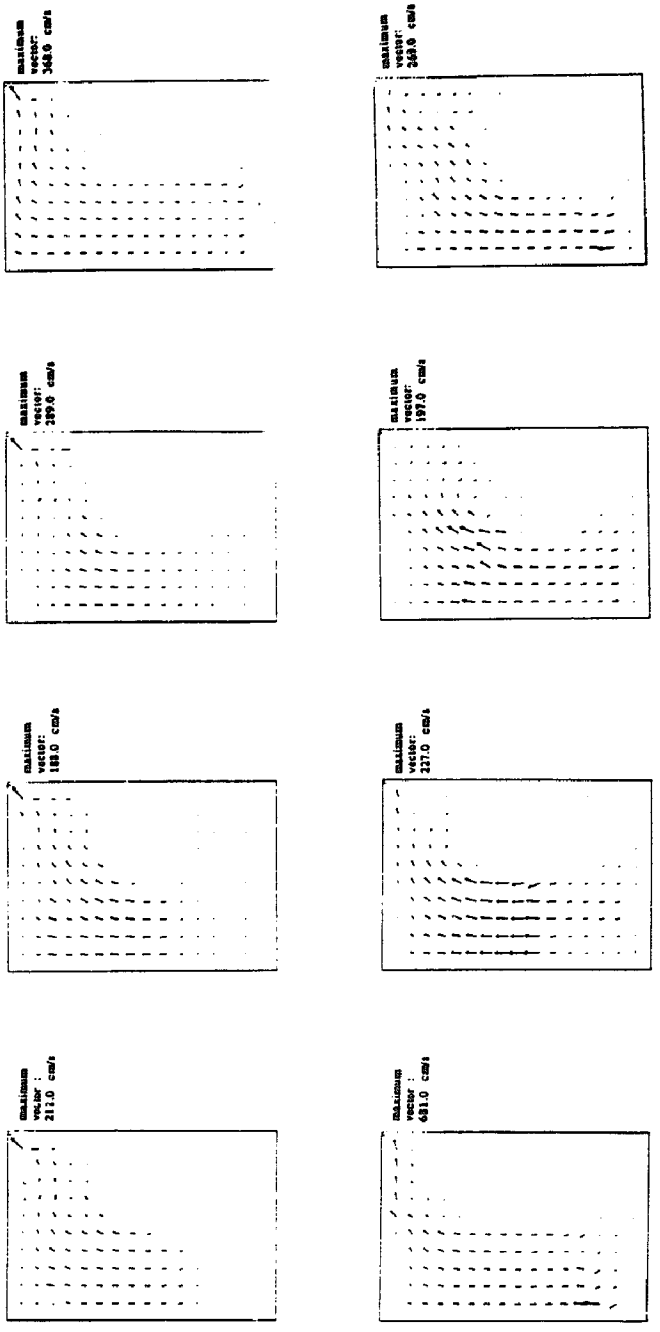
maximum vector: 348.0 cm/s
maximum vector: 268.0 cm/s
maximum vector: 299.0 cm/s
maximum vector: 197.0 cm/s
maximum vector: 188.0 cm/s
maximum vector: 227.0 cm/s
maximum vector : 211.0 cm/s
maximum vector : 481.0 cm/s

Fig. 3(a) (cont.).

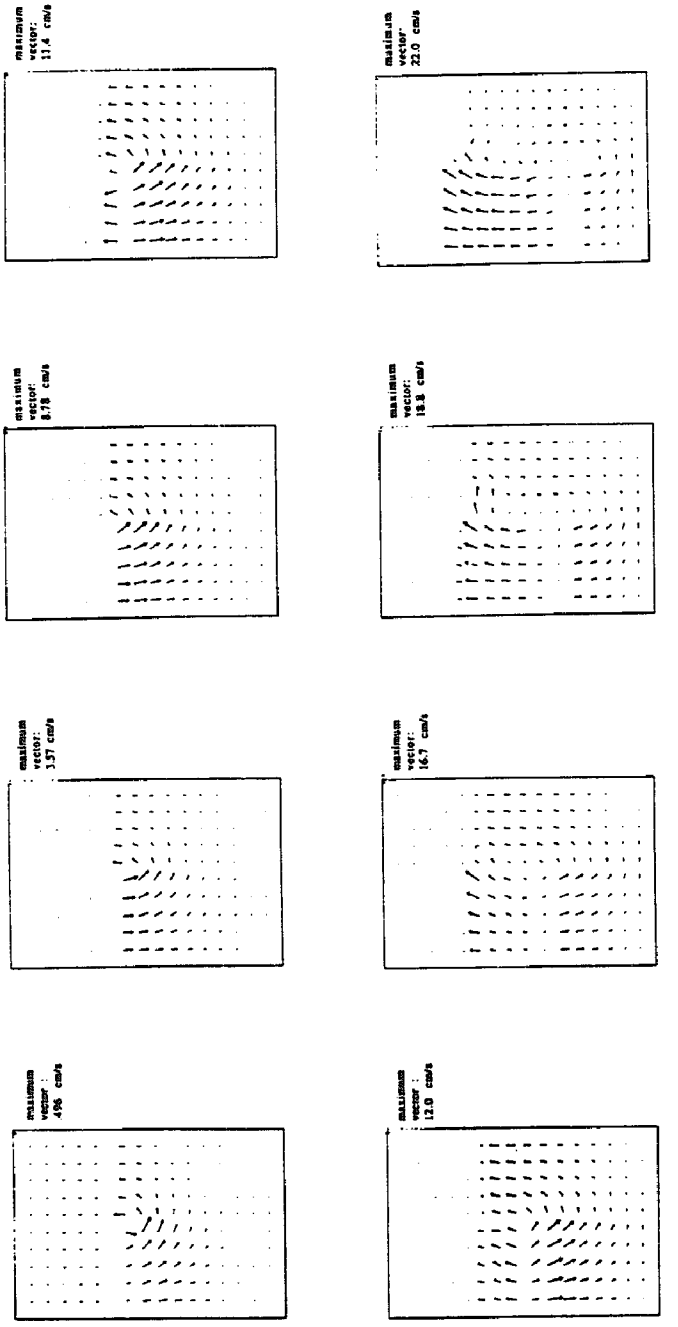
maximum vector: 11.4 cm/s
maximum vector: 22.0 cm/s
maximum vector: 8.78 cm/s
maximum vector: 18.8 cm/s
maximum vector: 3.57 cm/s
maximum vector: 16.7 cm/s
maximum vector: 4.96 cm/s
maximum vector: 12.0 cm/s

Fig. 3(b).

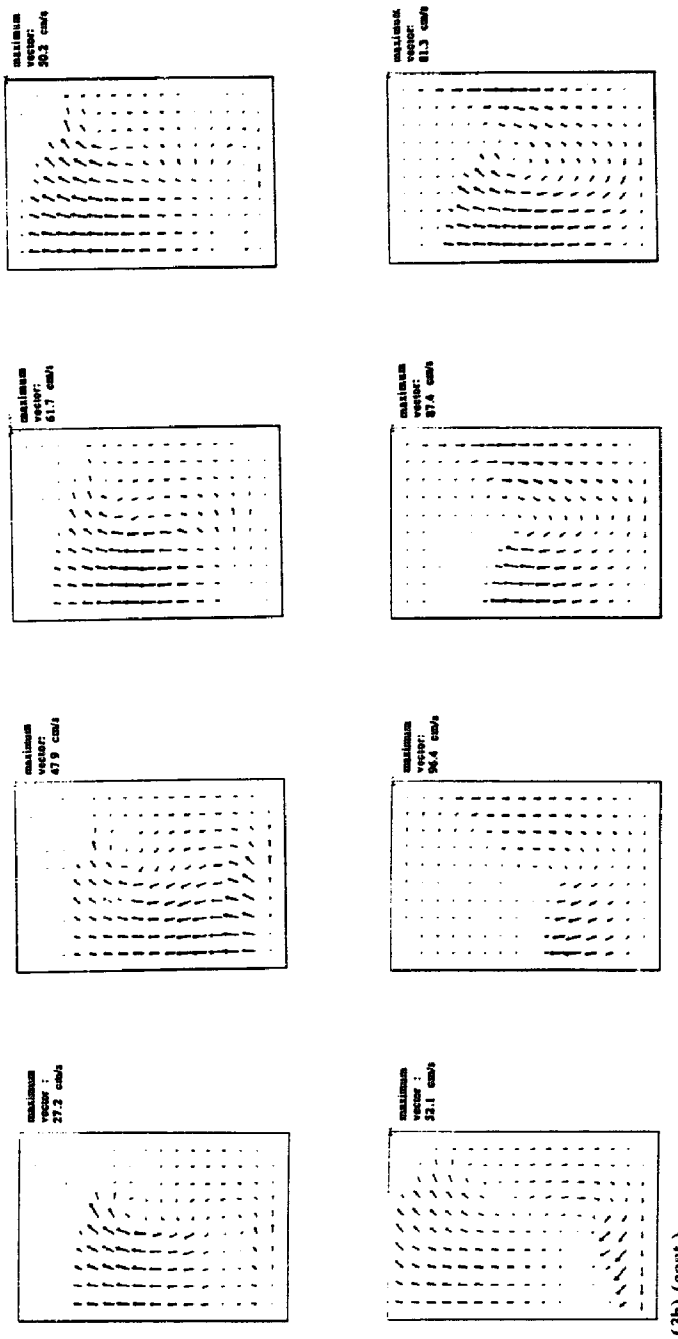

Fig. (3b) (cont.)

Fig. 3. Evolution of steam volume flux in numerical simulation of run no. 702. (a) Upper two rows, times (from impact of balls on the water) are 0.004 s, 0.054 s, 0.104 s, 0.154 s, 0.204 s, 0.254 s, 0.304 s, 0.354 s; lower two rows, times (from impact of balls on the water) are 0.404 s, 0.454 s, 0.504 s, 0.554 s, 0.604 s, 0.654 s, 0.704 s, 0.754 s. (b) Upper two rows, times (from impact of balls on the water) are 0.004 s, 0.054 s, 0.104 s, 0.154 s, 0.204 s, 0.254 s, 0.304 s, 0.354 s; lower two rows, times (from impact of balls on the water) are 0.404 s, 0.454 s, 0.504 s, 0.554 s, 0.604 s, 0.654 s, 0.704 s, 0.754 s.

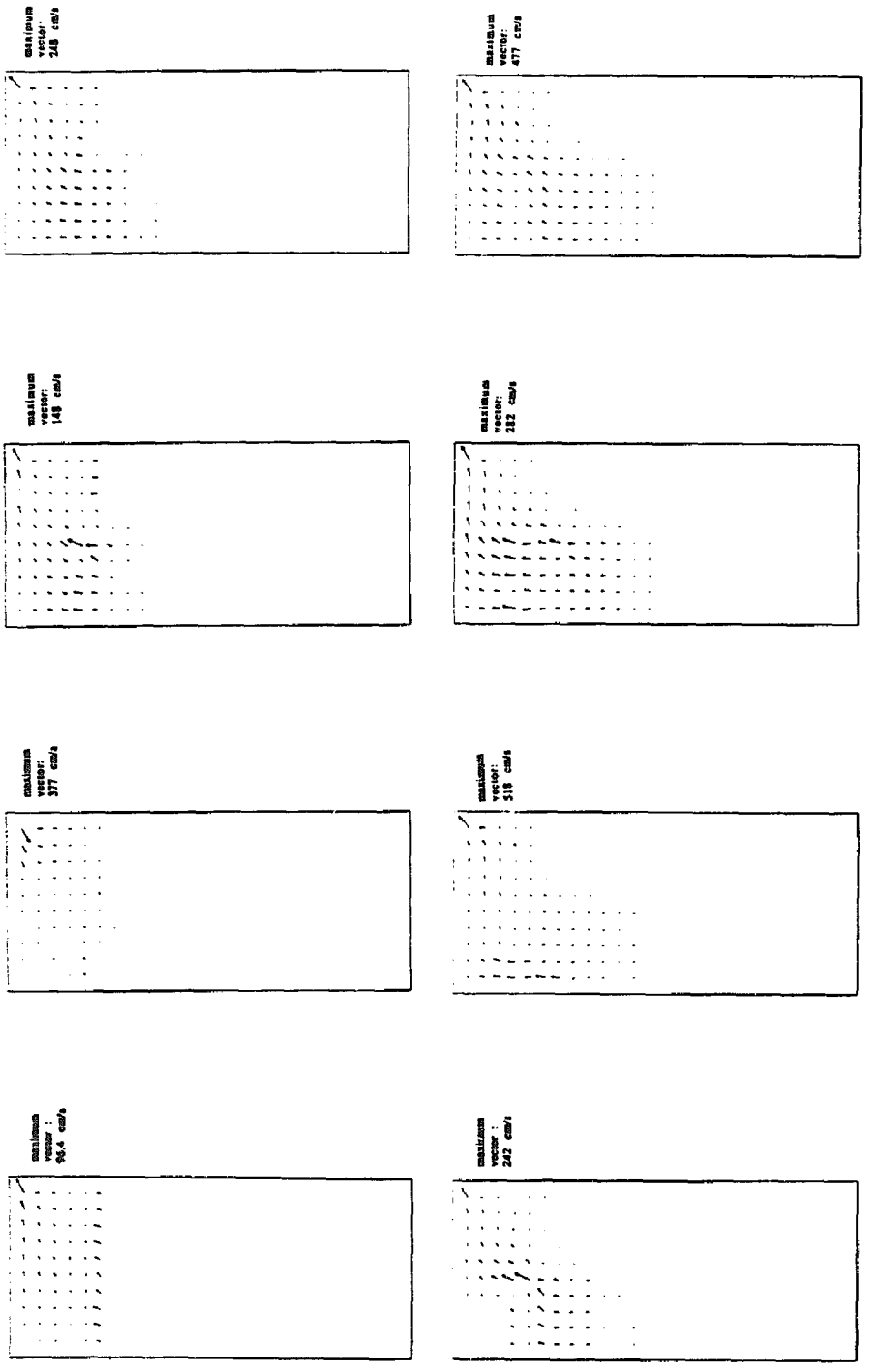
maximum vector: 248 cm/s
maximum vector: 477 cm/s
maximum vector: 149 cm/s
maximum vector: 312 cm/s
maximum vector: 377 cm/s
maximum vector: 518 cm/s
maximum vector: 96.4 cm/s
maximum vector: 242 cm/s

Fig. 4(a).

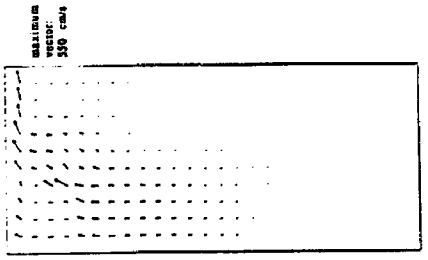
maximum
vector:
550 cm/s

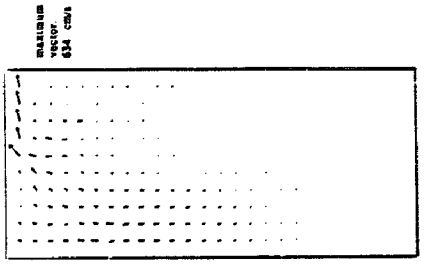
maximum
vector:
634 cm/s

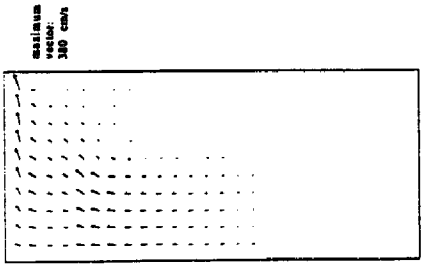
maximum
vector:
380 cm/s

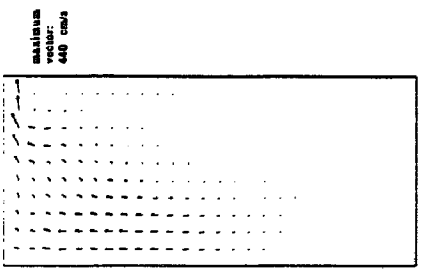
maximum
vector:
440 cm/s

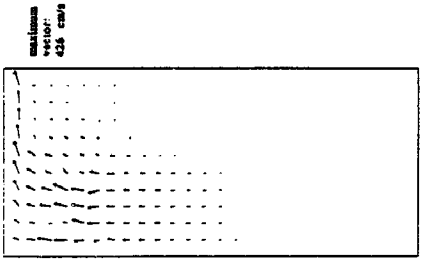
maximum
vector:
426 cm/s

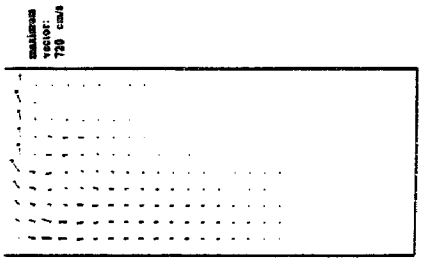
maximum
vector:
720 cm/s

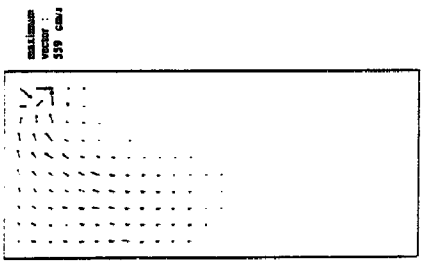
maximum
vector :
559 cm/s

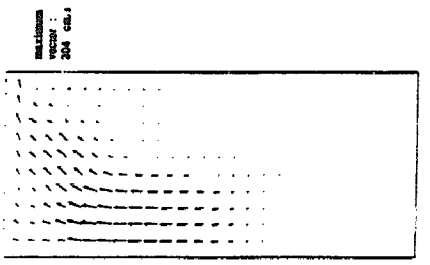
maximum
vector :
304 cm/s

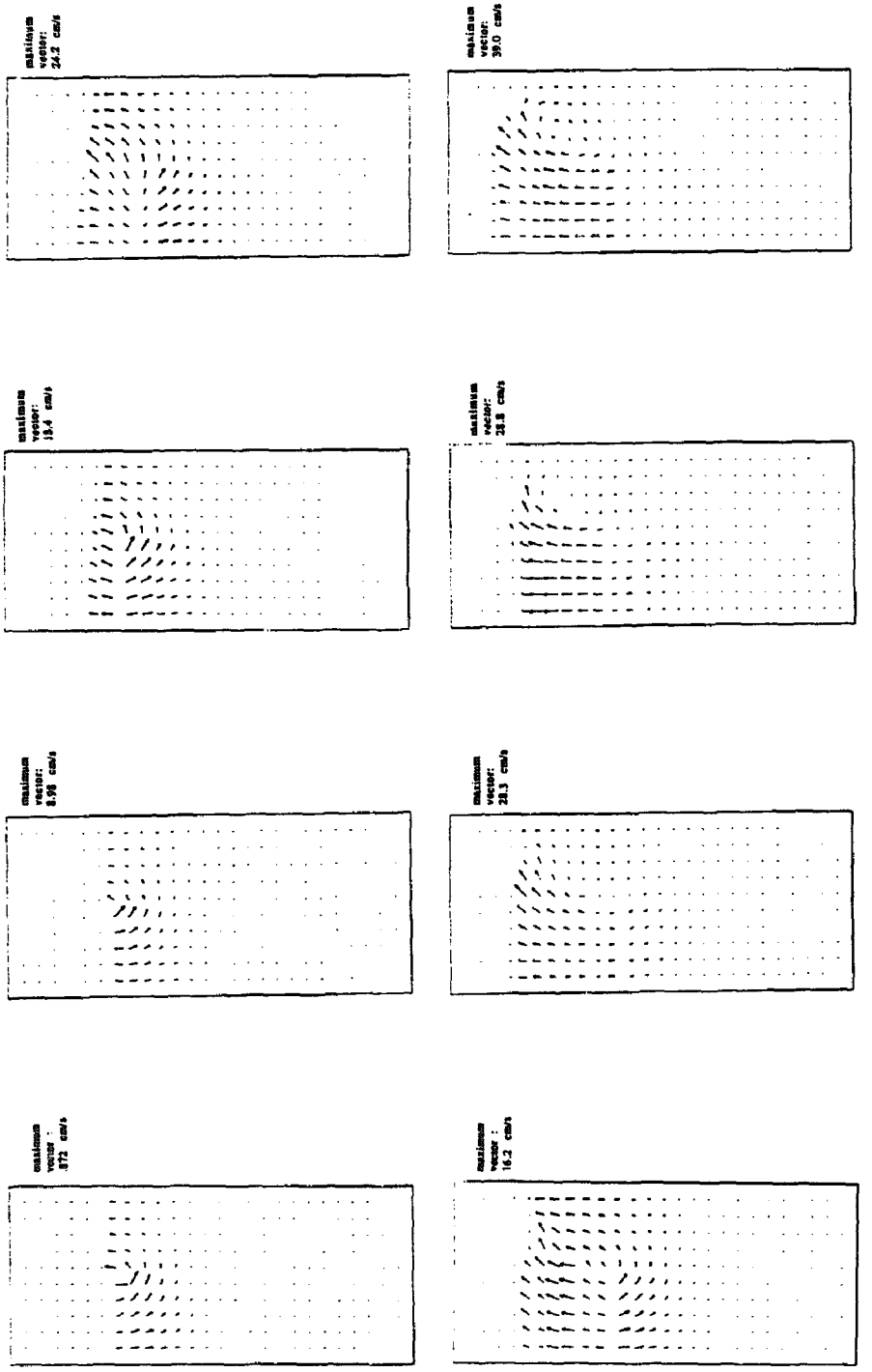
maximum vector: 24.2 cm/s
maximum vector: 39.0 cm/s
maximum vector: 18.4 cm/s
maximum vector: 28.8 cm/s
maximum vector: 8.98 cm/s
maximum vector: 28.3 cm/s
maximum vector : 372 cm/s
maximum vector : 16.2 cm/s

Fig. 4(b).

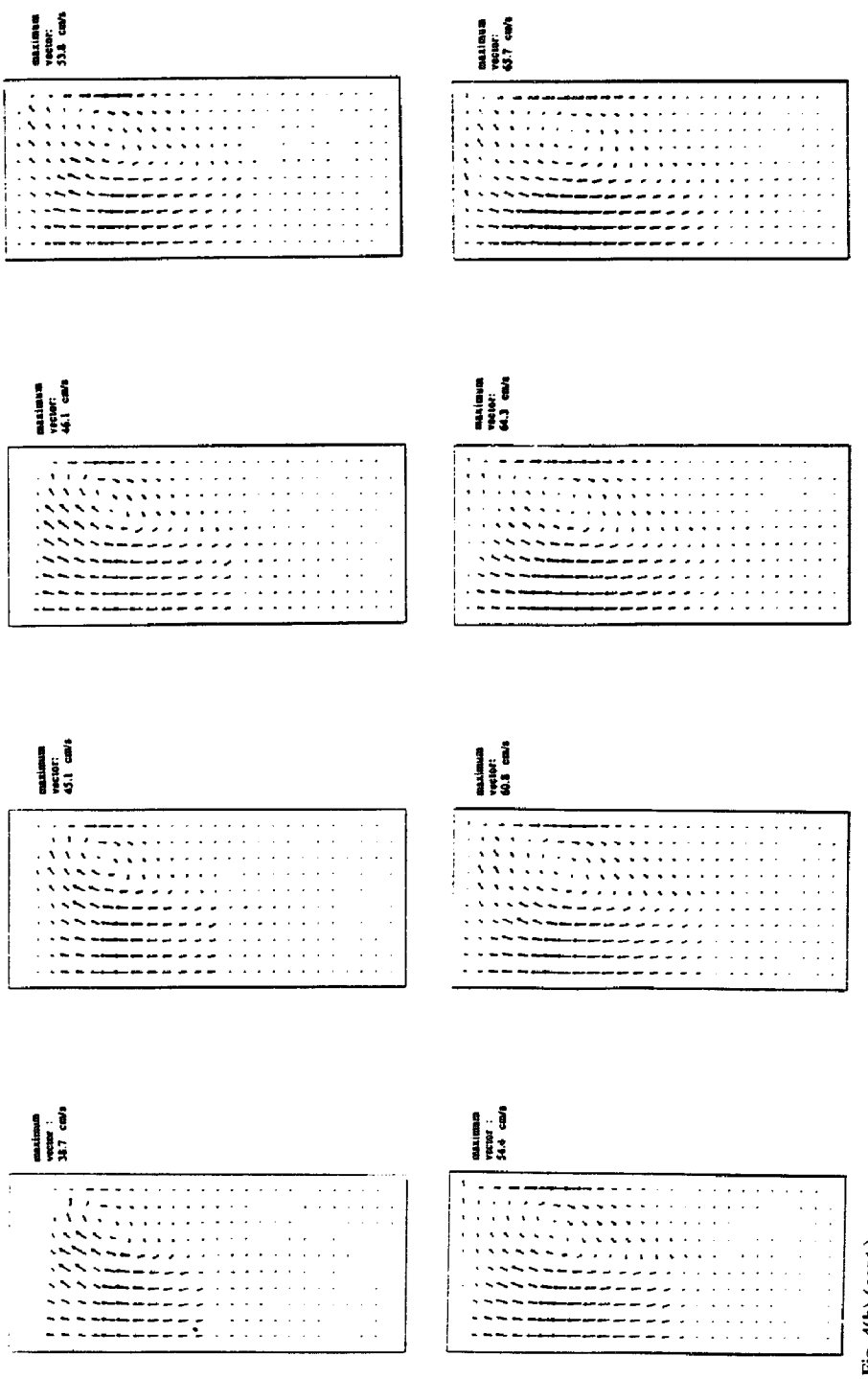

Fig. 4(b) (cont.).

Fig. 4. Evolution of steam volume flux in numerical simulation of run no. 905. (a) Upper two rows, times (from impact of balls on the water) are 0.004 s, 0.054 s, 0.104 s, 0.154 s, 0.204 s, 0.254 s, 0.304 s, 0.354 s; lower two rows, times (from impact of balls on the water) are 0.404 s, 0.454 s, 0.504 s, 0.554 s, 0.604 s, 0.654 s, 0.704 s, 0.754 s. (b) Upper two rows, times (from impact of balls on the water) are 0.004 s, 0.054 s, 0.104 s, 0.154 s, 0.304 s, 0.354 s; lower two rows, times (from impact of balls on the water) are 0.404 s, 0.454 s, 0.504 s, 0.554 s, 0.604 s, 0.654 s, 0.704 s, 0.754 s.

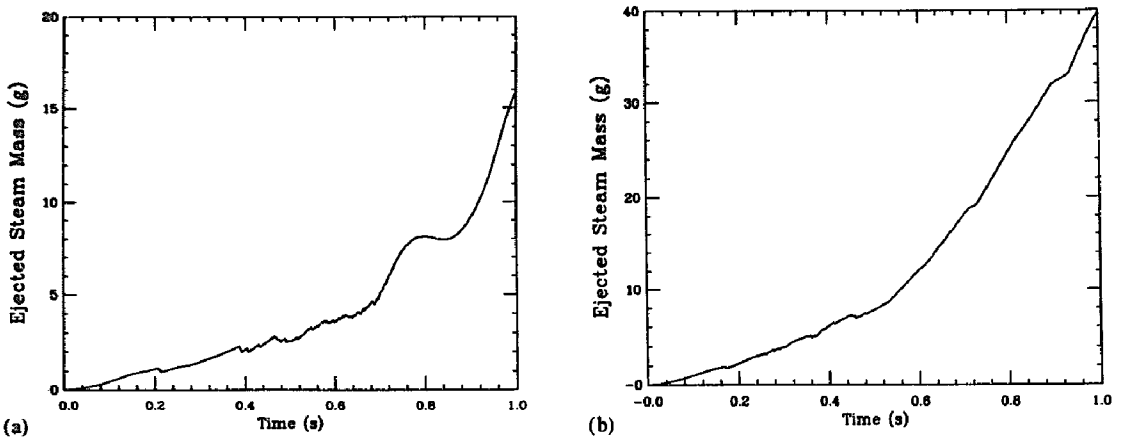

Fig. 5. Mass of steam ejected through venting cell in numerical simulation of (a) run no. 702; (b) run no. 905.

water volume flux patterns for the conditions of MAGICO runs no. 702 (25-cm pool, 2.4-mm balls, 800 °C) and no. 905 (50-cm pool, 1.5-mm balls, 800 °C). These runs were chosen for the purpose of explaining the prediction of a "reversal of water volume flux" phenomenon which we believe relates to, and explains, an experimentally found sudden increase in steam generation rate under certain conditions during the premixing transient. More specifically, we believe that reversal of water flux causes a strong counter-current melt–water contact and an associated rapid increase in steam generation rates; accordingly, the resulting phenomenon is termed energetic transfer of heat in a counter-current ambient (ETHICCA).

The reversal of water volume flux is illustrated in Figs. 3 and 4 for runs no. 702 and no. 905, respectively. (In these figures, spatial maps are given for only one-half of the flow field symmetry.) In the initial stages, we can see that the generated steam moves upward and out of the mixing region, while the water is being pushed down and to the sides. This creates a counterclockwise motion in the liquid around the mixing zone. As time goes on, the behavior of the steam remains basically the same, except for being lifted from farther down the pool in a pattern that follows the particle cloud front penetrating the pool. However, the water volume flux undergoes two major changes, one at 0.2 and the other at 0.6 s. At 0.2 s in the interaction, water is seen to begin to move upward within the mixing zone, apparently being "lifted" by the steam flow. The mixing region is therefore becoming depleted of liquid for three reasons: vaporization, water being pushed down and to the sides by the particles, and water being lifted by the steam. The implied internal stagnation region is clearly visible in Figs. 3(b) and 4(b). The other change occurs around 0.6 s, when the water around the mixing zone reverses sense of "rotation" (note that these are all irrotational motions) and begins to flow into the mixing zone! At about the same time with this flow reversal, the high-speed movies show a relatively violent breakup of the pool surface, as if by a suddenly increased steam generation rate; this is the ETHICCA connection mentioned above. Quantitatively, this sudden change in steaming rate is illustrated in Figs. 5(a,b), and in detail is seen to depend on particle size and pool depth, and we expect on particle temperature also. However, we believe that the most important parameter affecting ETHICCA is the pour-to-pool diameter ratio, and in the limit to where this ratio is 1, ETHICCA should vanish; preliminary calculations confirm this expectation. The particular mechanism, in elementary terms, is due to the buildup of gravitational head between the inside

(a)

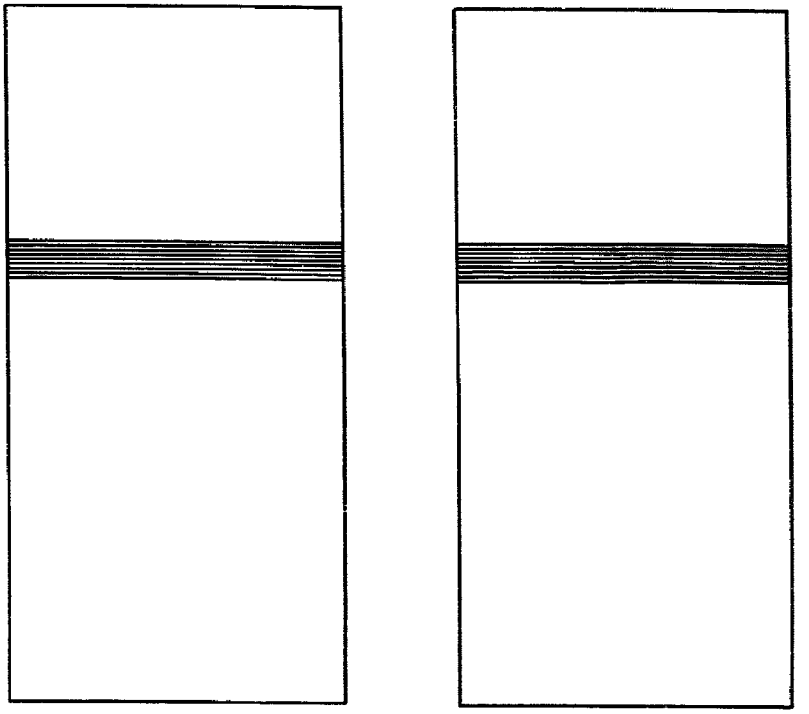

(b)

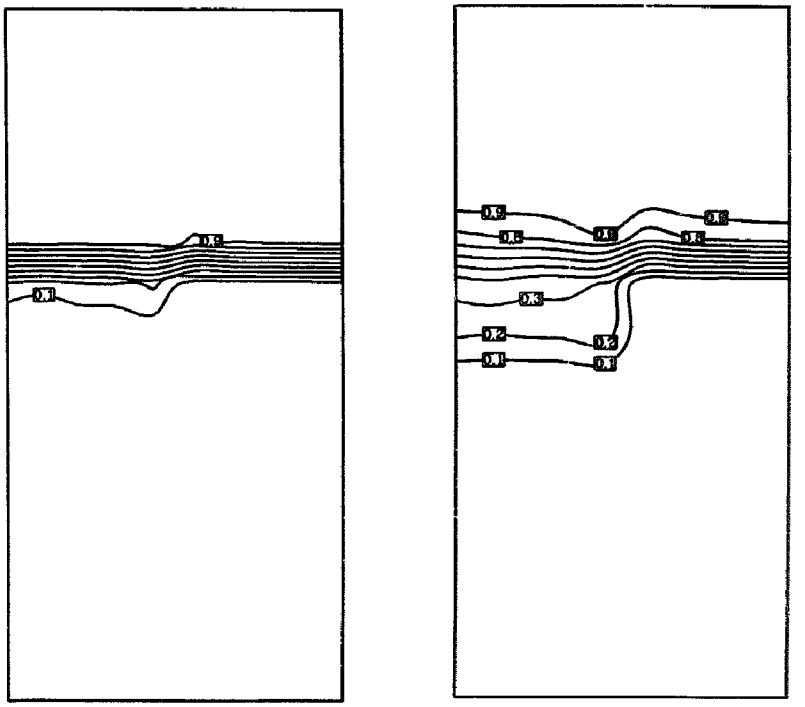

(c)

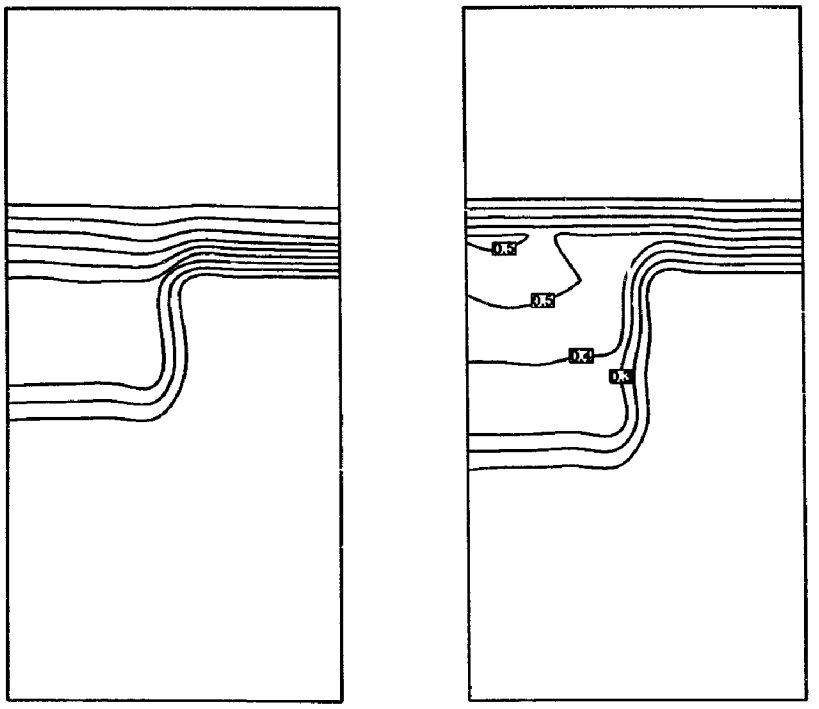

(d)

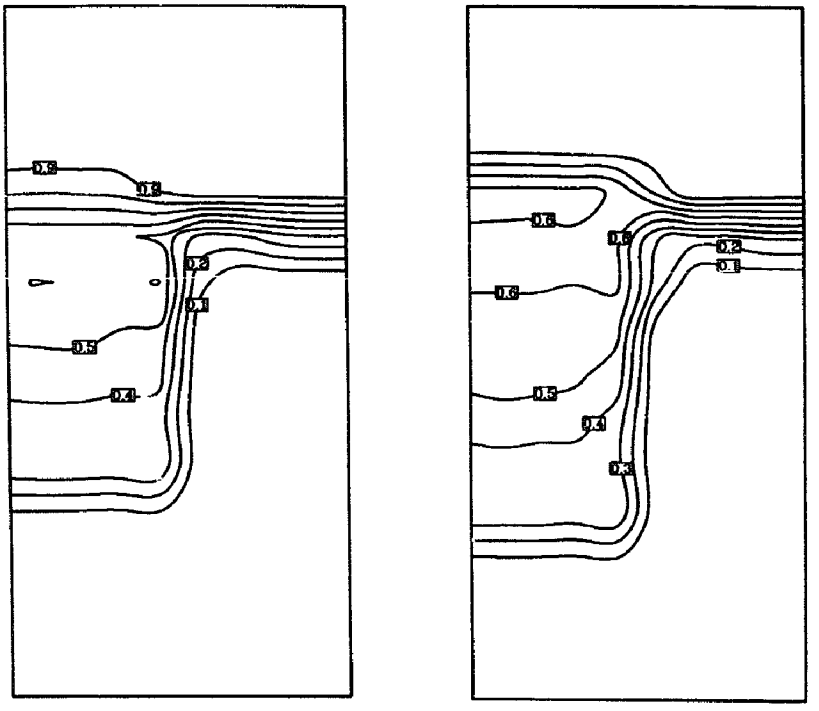

(e)

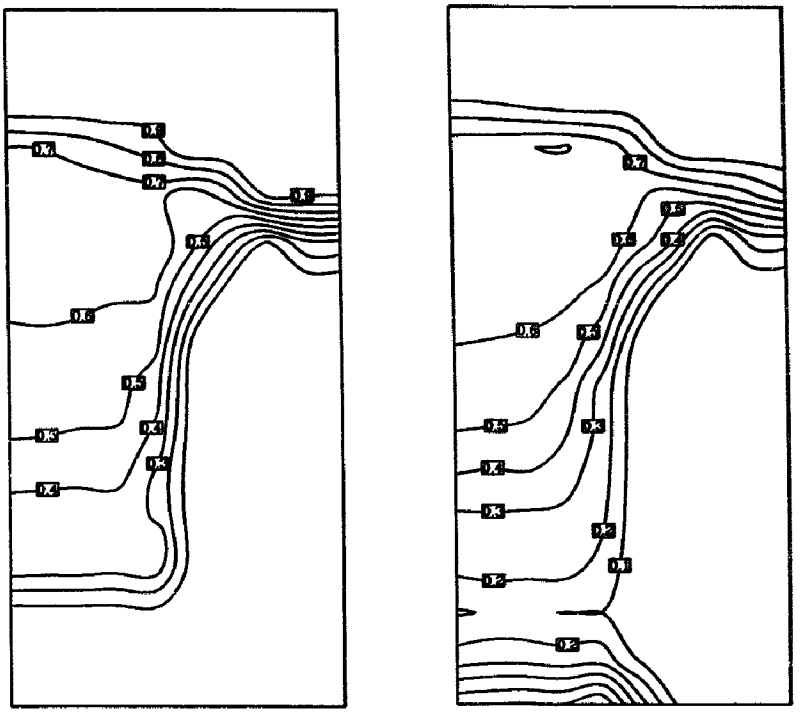

(f)

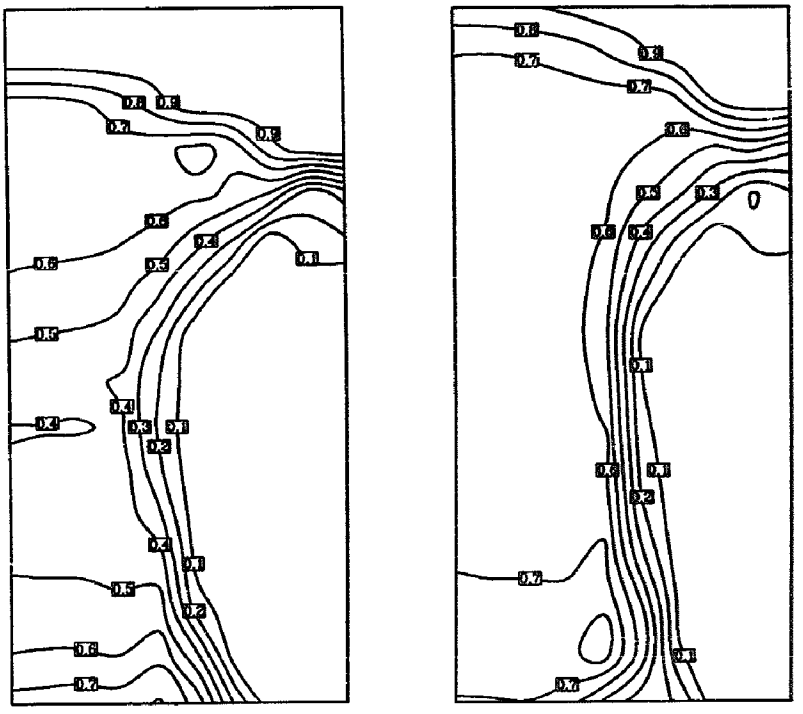

(g)

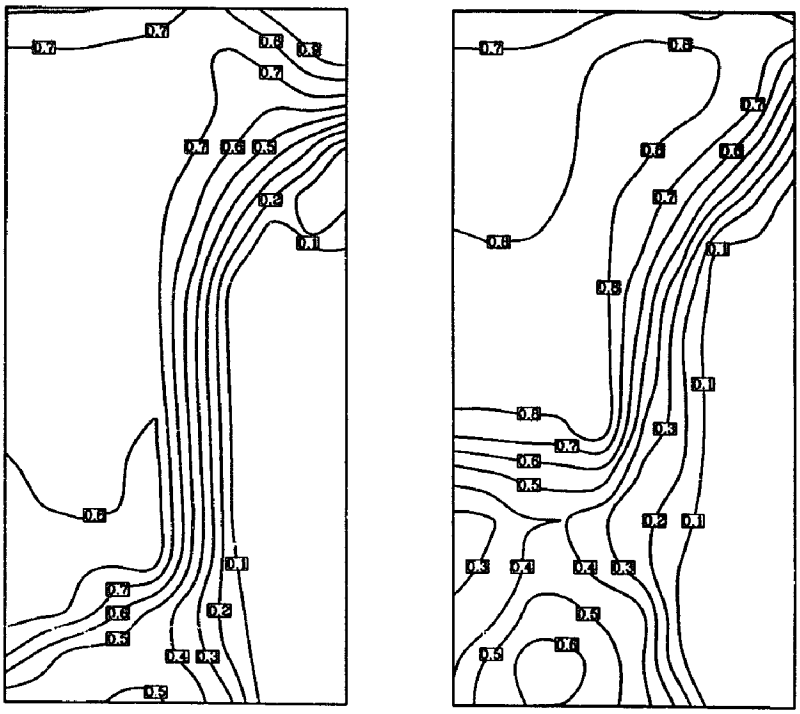

(h)

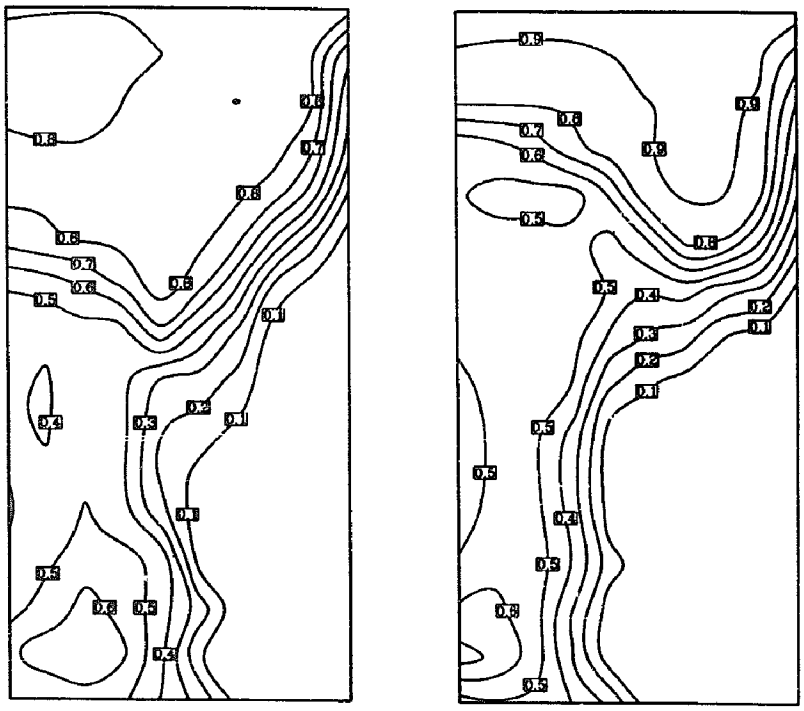

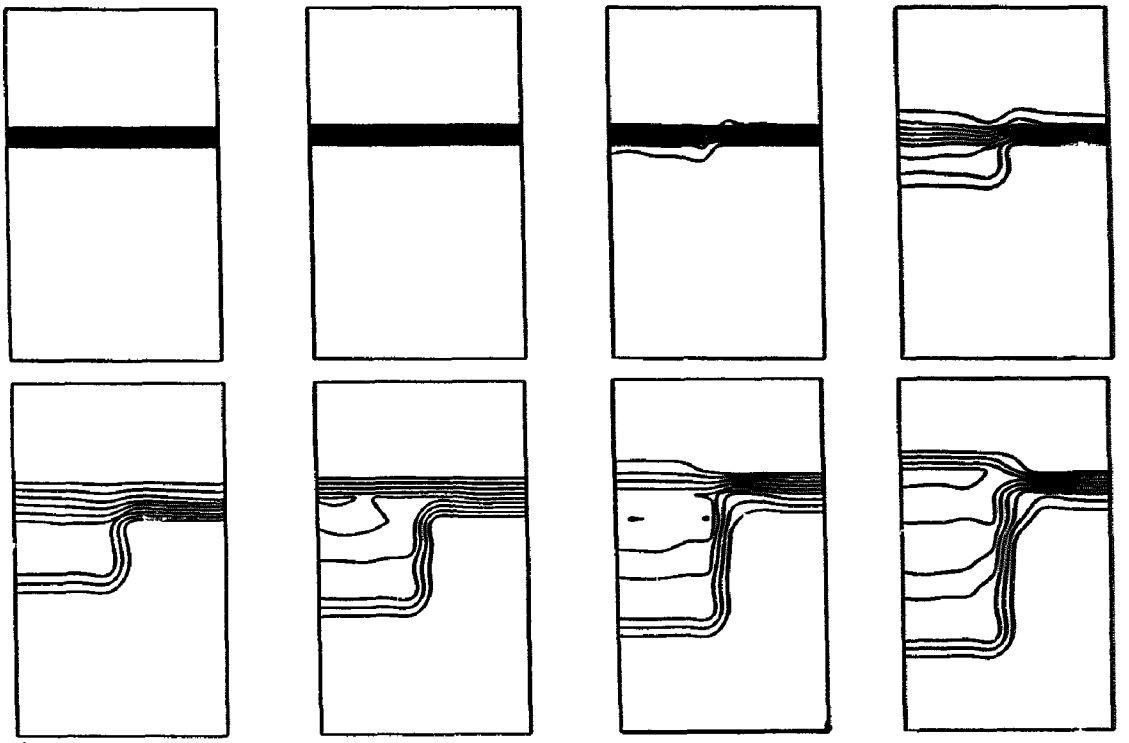

(i)

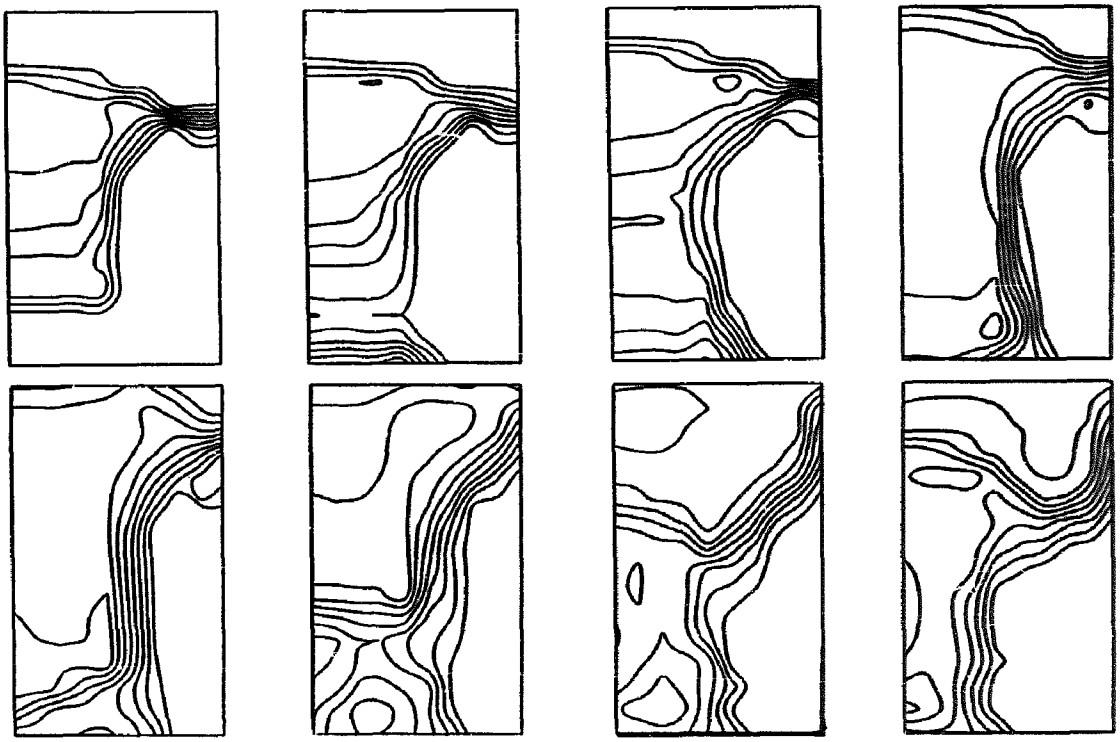

(j)

(voiding) of the mixing zone and the outside water (hence, absolute value of water pool depth is also important), and is another manifestation of the decisively non-one-dimensional nature of premixing transients.

Apart from the water volume flux evolution, the ETHICCA can be tracked from the evolution of the steam volume fraction in time. This is shown in Figs. 6 and 7 for runs no. 702 and no. 905, respectively. These figures are given in two forms, a synoptic one in Figs. 6i,j and 7i,j for visualizing the whole transient, and a quantitative one in Figs. 6a–h and 7a–h with the void fraction contours labelled. From these figures, we can visualize the growth of the mixing zone and the breakup associated with ETHICCA. In addition, they may be seen to be remarkably similar (in shapes) to sample snapshots taken during actual runs and collected in Figs. 8 and 9. In particular, notice the agreement in the violent breakup of the pool surfaces seen to occur at around 0.4 s in run no. 905.

To conclude, it would appear interesting now to carry out more focused investigations suggested by these results; specifically by measuring velocity profiles in the water surrounding the interaction zone, and by visualizing the internal (void fraction) shapes within the zone itself (see Appendix B). Both are well within the technology currently available for MAGICO, and such studies are planned for the near future. Incidentally, we also plan experiments with aluminum oxide particles (different density than the steel ones used until now) of much higher temperatures. Finally, in a companion experimental/analytical program, we are studying film boiling from spheres in steam–water two-phase flows including conditions of elevated pressures (Liu, 1992).

6. Consideration of the FARO experiment

This experiment involves the pouring, under gravity, of tens-of-kilograms quantities of UO_2/ZrO_2 melts at high temperatures (~ 2700 °C) into deep water pools (~ 1 m) at high pressure (~ 5 MPa). The interaction is contained in a closed cylindrical vessel ~ 3 m in length and 0.47 or 0.71 m in diameter for the scoping test (ST) and the quenching test 2 (QT2), respectively. The initial pool temperature is well-characterized, and the water depth is given as 0.87 and 1 m for the ST and QT2, respectively. Thus, the flow field can be simply represented for simulations with PM-ALPHA, as illustrated in Fig. 10. The length of the gas space was slightly reduced to preserve the total test vessel volume (accounting for the melt catcher volume in it) to the values of 0.64 and 1.3 m^3 given for the ST and QT2 conditions, respectively. This whole flow field was discretized, uniformly, into 5 radial and 60 axial cells ($\Delta r = 4.7$ cm, $\Delta z = 6.1$ cm). Cylindrical symmetry was assumed.

The only aspects of the simulations that require some elaboration are concerned with melt delivery, with certain transient behavior prior to the melt reaching the water pool surface, and with melt breakup in the interaction. The discussion of these aspects is limited here to the case of the scoping test, as only this test could be analyzed in the short time available since the release of these data (Magallon, 1992). However, the treatment is expected to be similar to the QT2 simulations that will follow in the near future

The melt delivery time is given as 0.28 s, for a total release of 18 kg of melt. Using this release rate and the melt-exit nozzle diameter (10 cm), we find an inlet melt velocity of 1.07 m s^{-1}. Under free-fall, the melt front is found to have traveled 0.67 m by the time the tail-end of the pour is entering the gas space; the melt front at this time, 0.28 s after initiation of the pour, is still 1.15 m above the water pool surface. Based on this, the calculation is initialized at 0.28 s with the experimentally measured value of the pressure in the gas space (~ 5.1 MPa) and the fuel distributed along the indicated column in Fig. 10 with volume

Fig. 6. Evolution of steam volume fraction in numerical simulation of run no. 702. Times (from impact of balls on the water) are (a) 0.004 s, 0.054 s; (b) 0.104 s, 0.154 s; (c) 0.204 s, 0.254 s; (d) 0.304 s, 0.354 s; (e) 0.404 s, 0.454 s; (f) 0.504 s, 0.554 s; (g) 0.604 s, 0.654 s; (h) 0.704 s, 0.754 s; (i) 0.004 s, 0.054 s, 0.104 s, 0.154 s, 0.204 s, 0.254 s, 0.304 s, 0.354 s; (j) 0.404 s, 0.454 s, 0.504 s, 0.554 s, 0.604 s, 0.654 s, 0.704 s, 0.754 s.

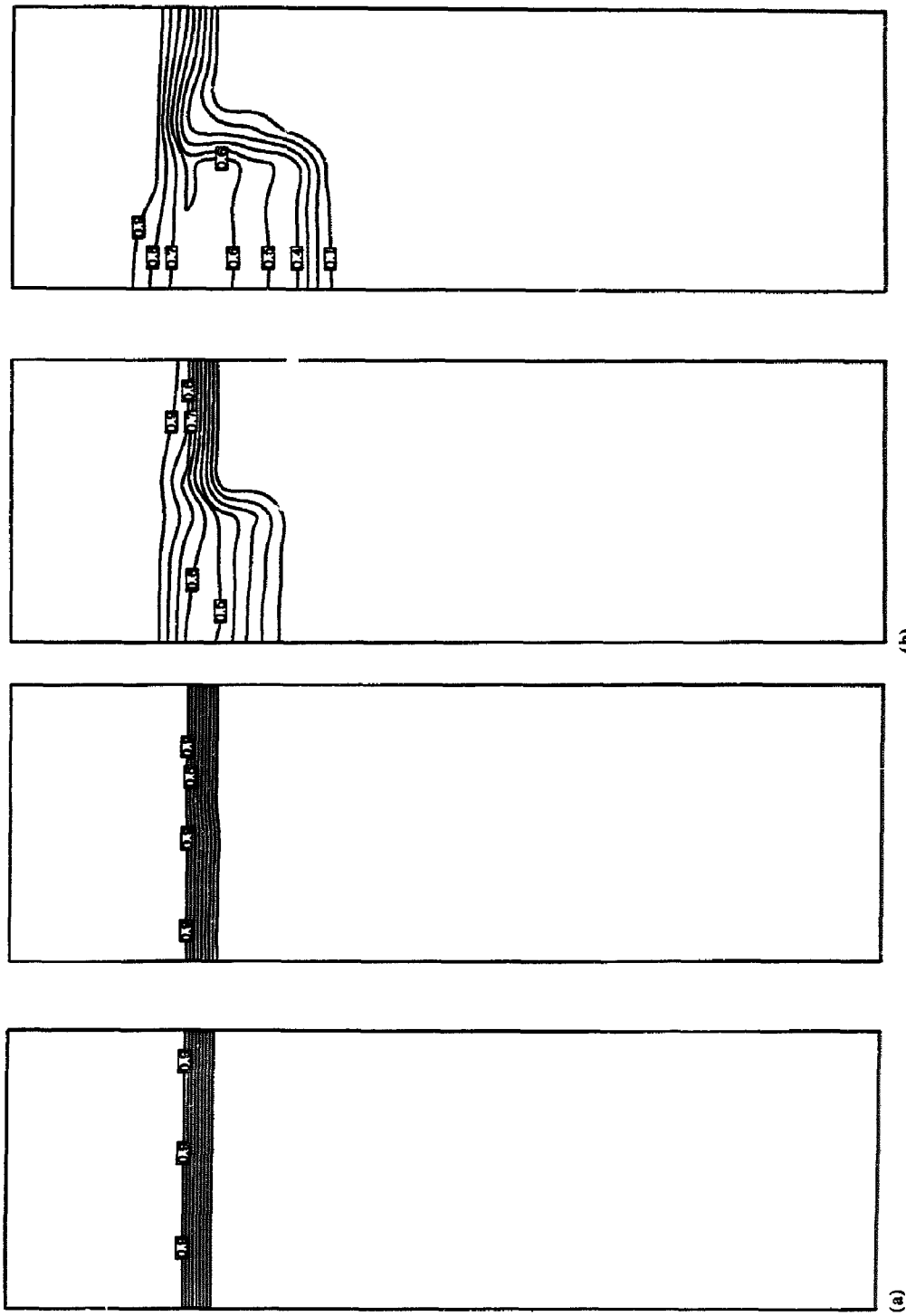

(b)

(a)

Fig. 7 (a and b).

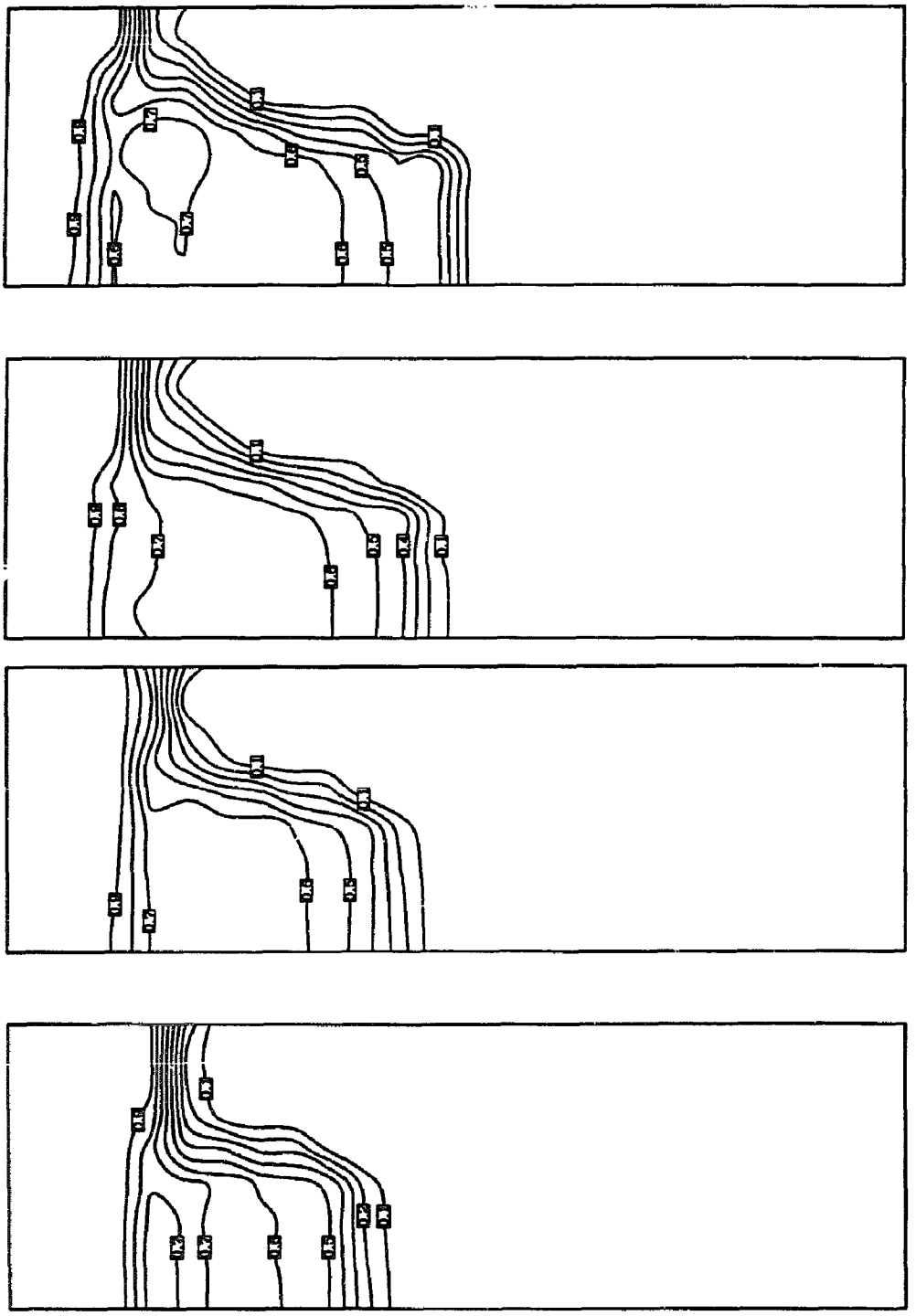

(d)

(c)

Fig. 7 (c and d).

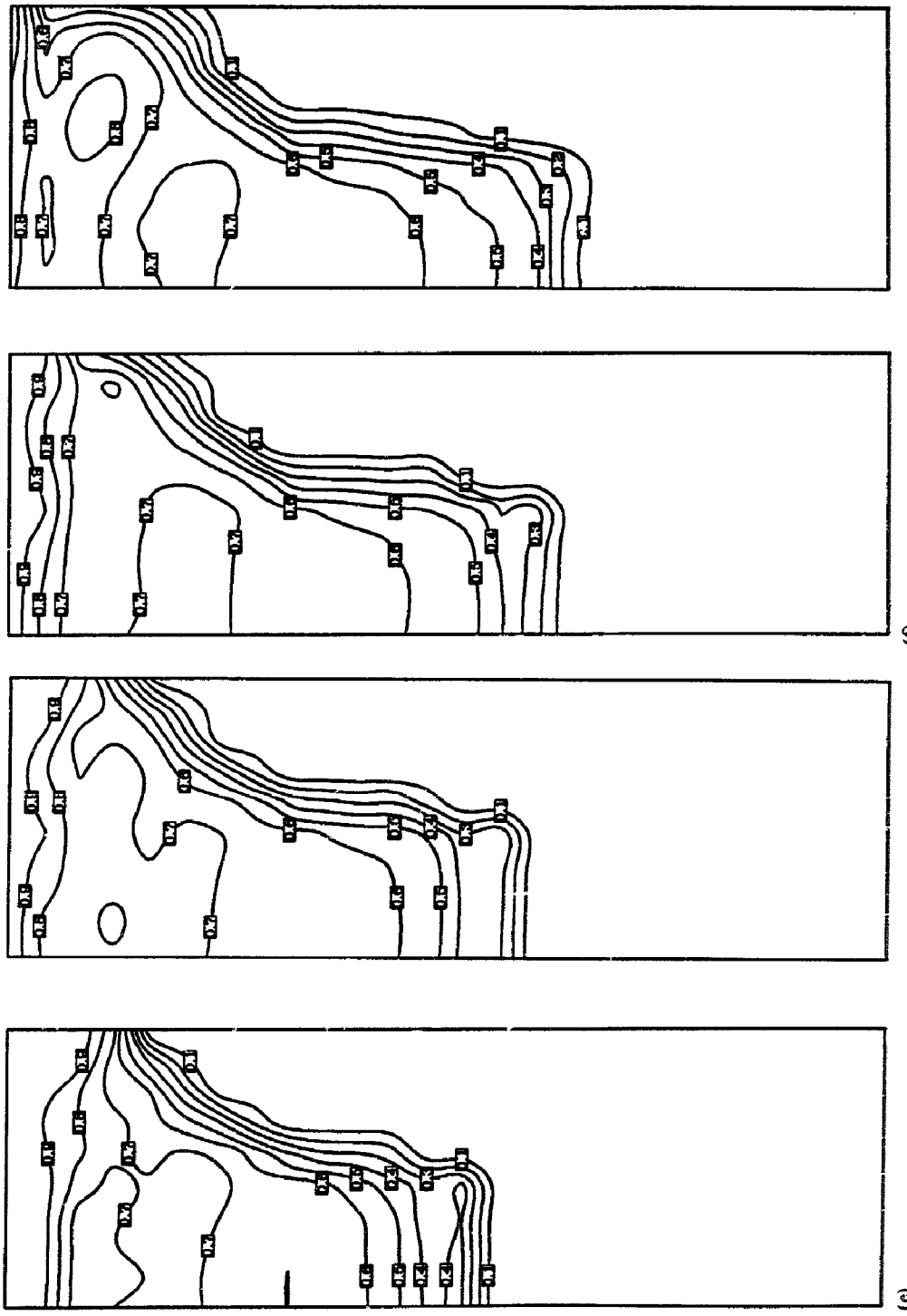

Fig. 7 (e and f).

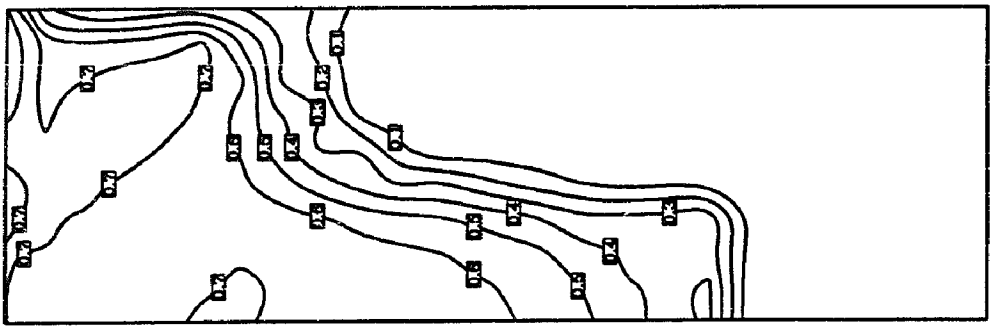

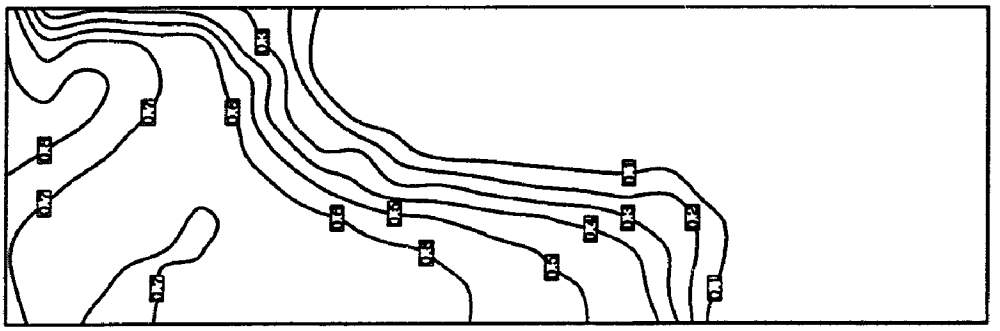

(h)

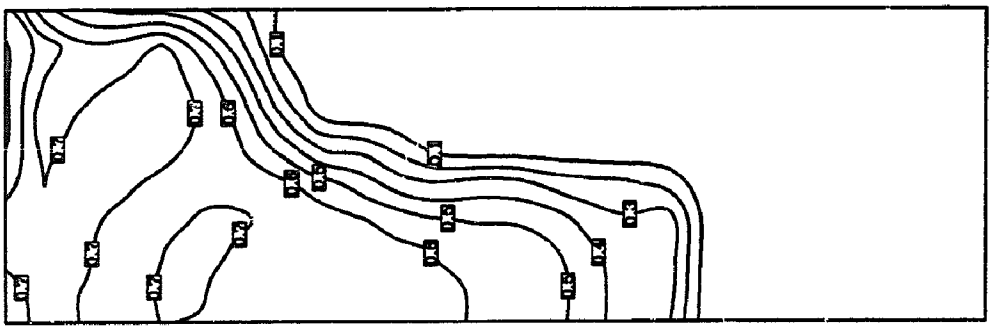

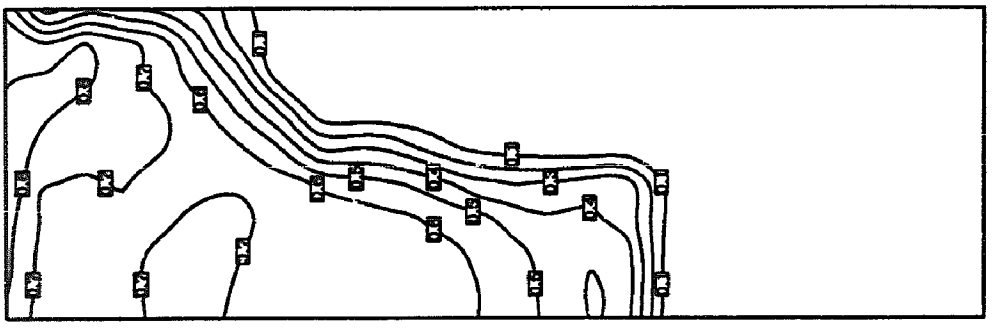

(g)

Fig. 7 (g and h).

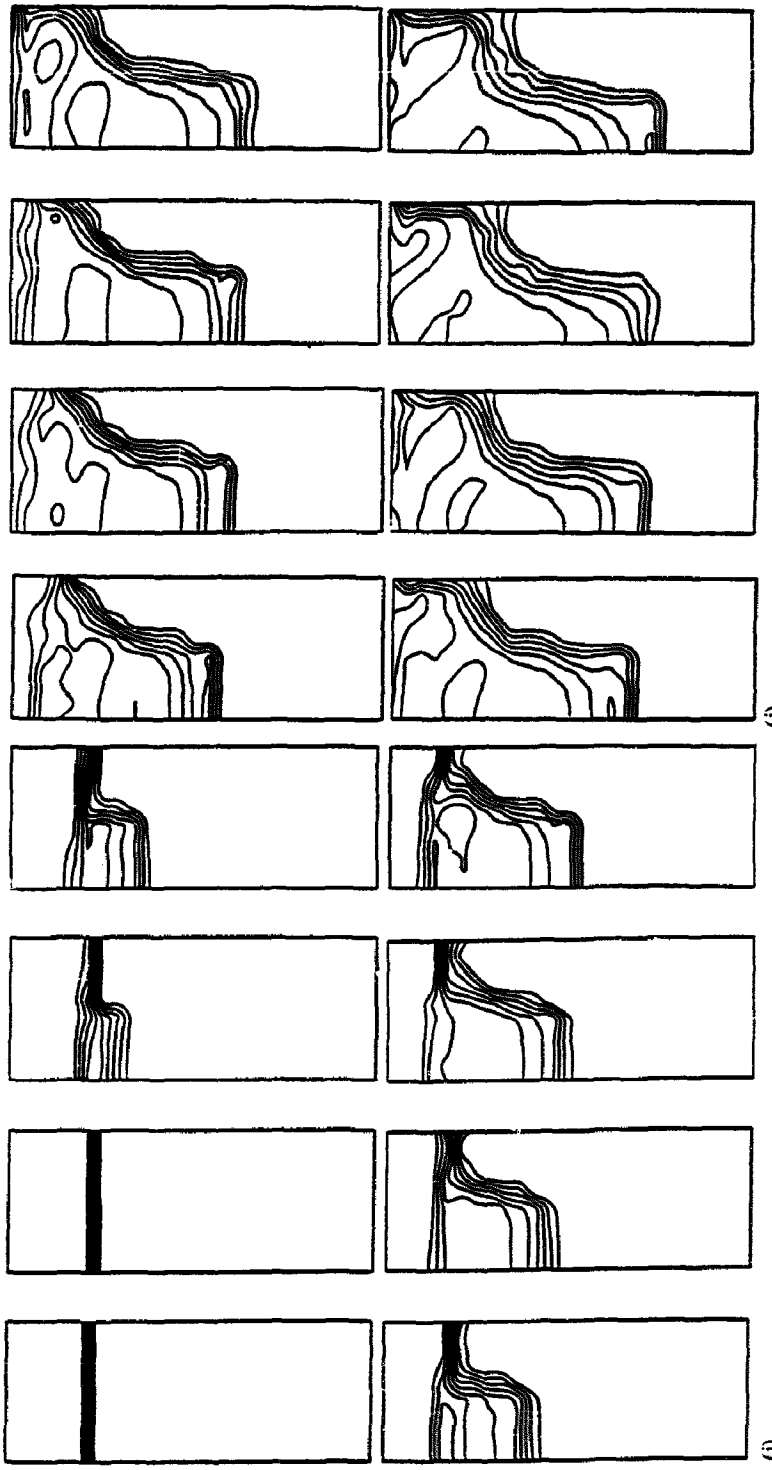

Fig. 7. Evolution of steam volume fraction in numerical simulation of run no. 905. Times (from impact of balls on the water) are (a) 0.004 s, 0.054 s; (b) 104 s, 0.154 s; (c) 0.204 s, 0.254 s; (d) 0.304 s, 0.354 s; (e) 0.404 s, 0.454 s; (f) 0.504 s, 0.554 s; (g) 0.604 s, 0.654 s; (h) 0.704 s, 0.754 s; (i) 0.004 s, 0.054 s, 0.104 s, 0.154 s, 0.204 s, 0.254 s, 0.304 s, 0.354 s; (j) 0.404 s, 0.454 s, 0.504 s, 0.554 s, 0.604 s, 0.654 s, 0.704 s, 0.754 s.

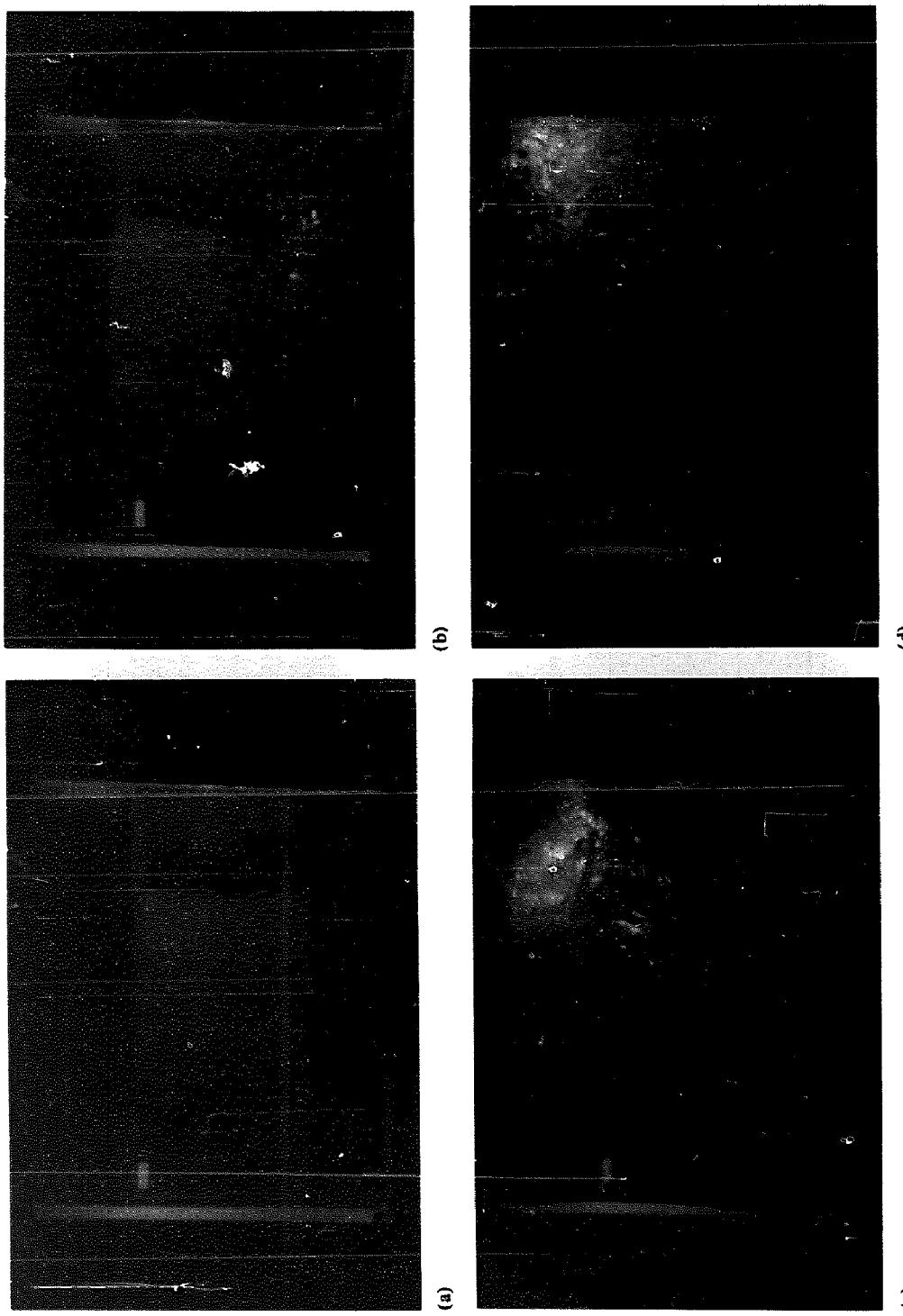

Fig. 8. Snapshots of run no. 205 (identical to run no. 702). Times (from impact of balls on the water) are (a) 0.27 s and (b) 0.57 s; (c) 0.87 s and (d) 1.17 s.

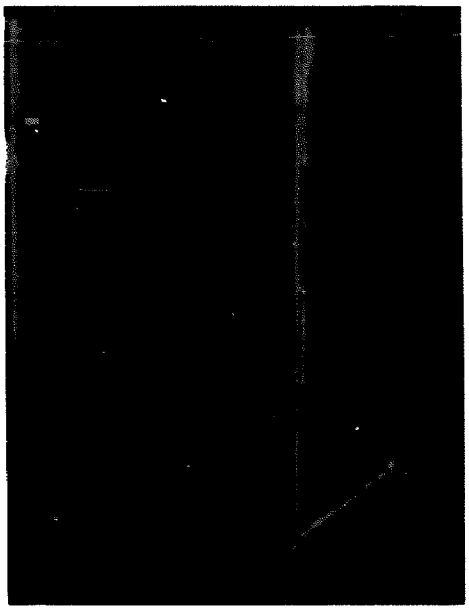

(a)

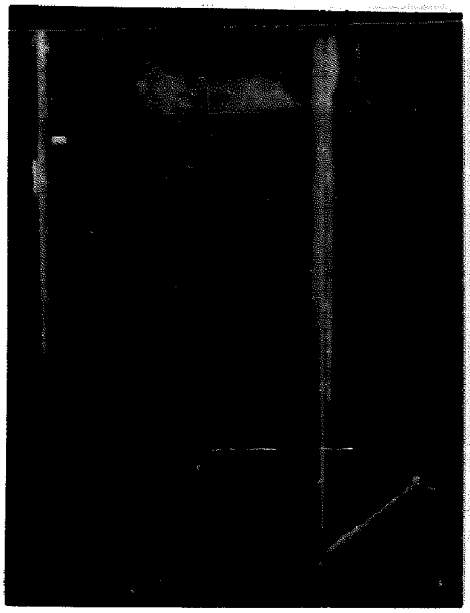

(b)

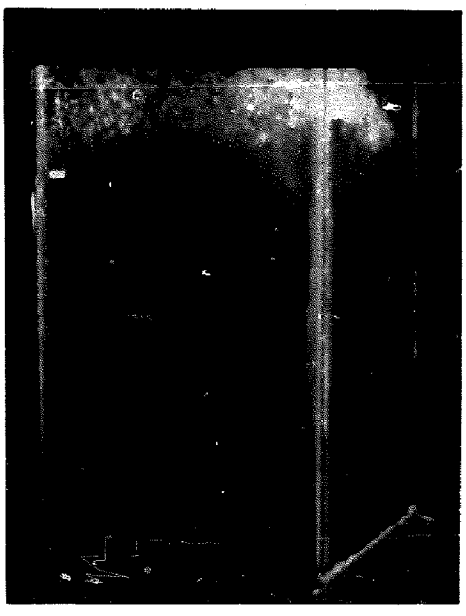

(c)

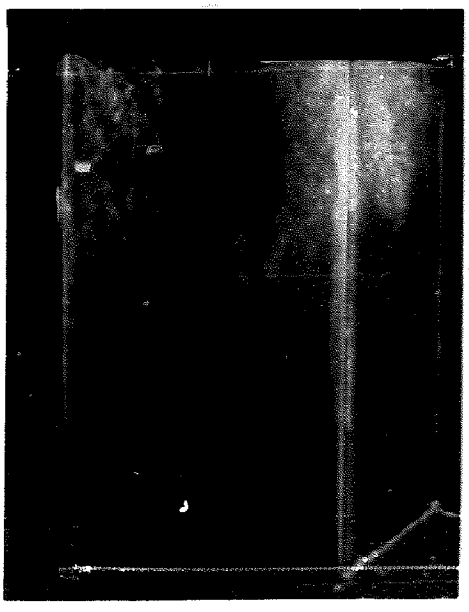

(d)

Fig. 9 (a–d).

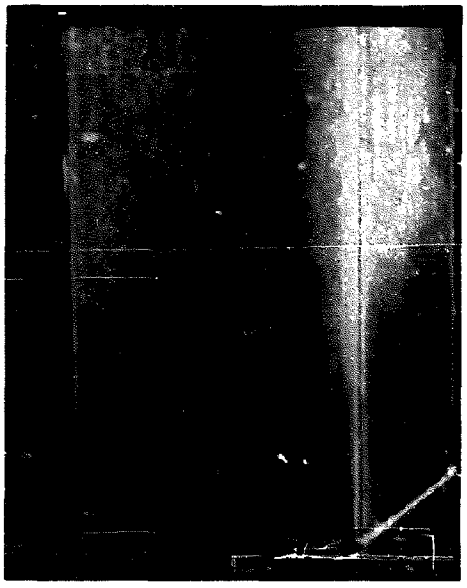

(e)

(f)

(g)

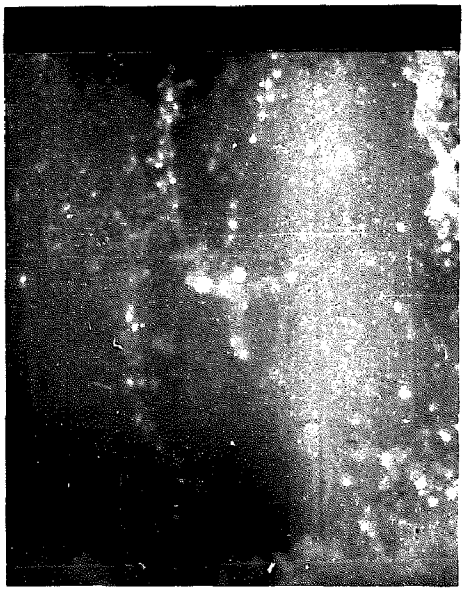

(h)

Fig. 9. Snapshots of run no. 905. Times (from impact of balls on the water) are (a) 0.1 s and (b) 0.4 s; (c) 0.7 s and (d) 1.0 s; (e) 1.3 s and (f) 1.6 s; (g) 1.9 s and (h) 2.8 s.

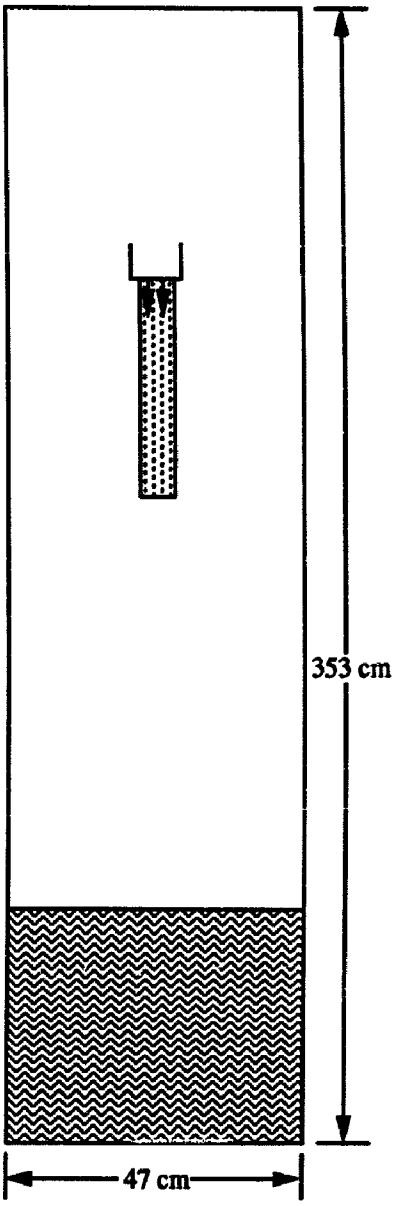

Fig. 10. Illustration of the flow field utilized in PM-ALPHA for the interpretation of the FARO experiment.

fractions and velocities in each cell obtained by accelerating the respective "parcel" under gravity, with the quoted initial velocity, in order to arrive at the respective location at the appropriately

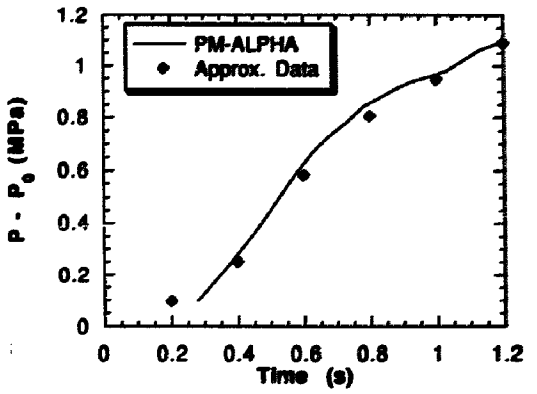

Fig. 11. Comparison of calculated pressure history with the FARO data from the scoping test.

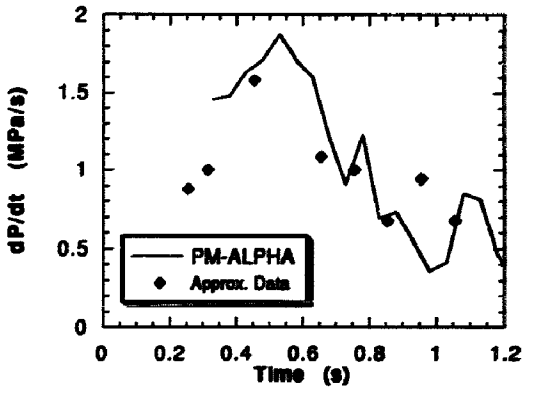

Fig. 12. Comparison of calculated pressurization rate with the FARO data from the scoping test.

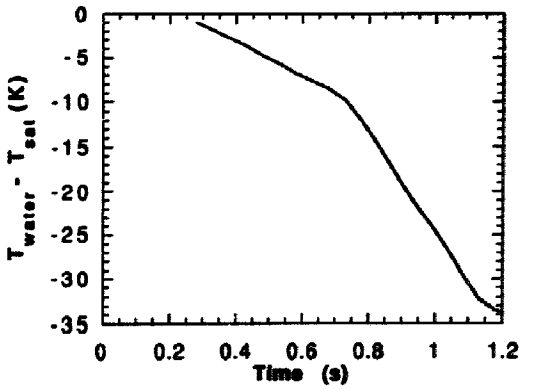

Fig. 13. Calculated buildup of water subcooling, as a result of the pressurization transient, at locations away from the mixing zone.

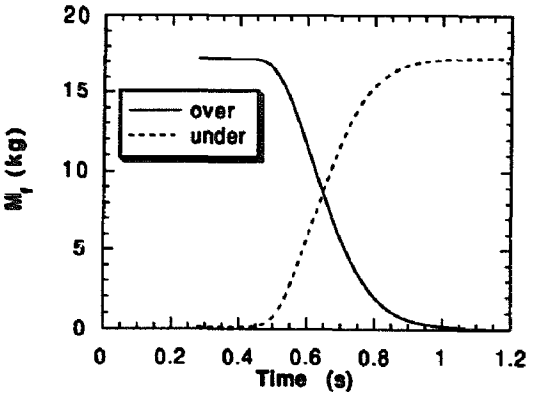

Fig. 14. The calculated "sinking" of the fuel "column into the water pool.

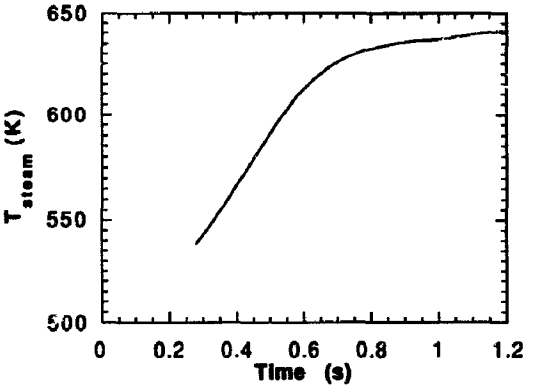

Fig. 16. Calculated temperature rise in a typical cell in the gas space away from the water surface.

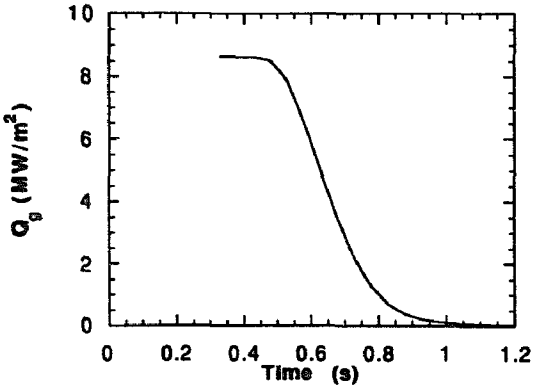

Fig. 15. Illustration of the diminishing of the radiative heat source to a typical cell in the gas space, as a consequence of the melt sinking, per Fig. 14.

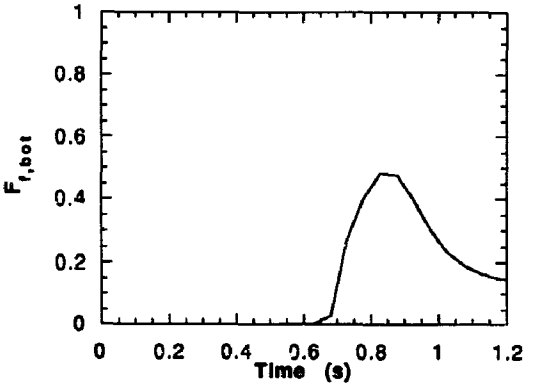

Fig. 17. Calculated arrival rate of melt into the melt catcher.

available travel time ($0 \leqslant t \leqslant 0.28$ s). Note that the innermost cell diameter is very nearly equal to that of the melt-exit nozzle; thus, all melt is taken to be contained within it.

The other aspect of the simulation that requires some elaboration is the treatment of melt-to-gas radiation heat transfer. This is peculiar to a closed system, with large cover-gas space, at high pressure, as is the case here, and its importance has already been noted by Magallon et al. (1992). An a priori treatment of this aspect would only be possible if the extent of melt breakup, and its emissivity, were known, which of course, is not the case. However, our interest in these tests is primarily on the melt-coolant interactions, and the melt-to-gas heat transfer is relevant only in providing the proper boundary conditions (subcooling induced due to pressurization) for this interaction. Our approach, therefore, is to sort out the melt-to-gas heat transfer from the early portion of the pressurization transient (prior to melt contacting the water) in such a way that it can be consistently "merged" with the fuel-coolant interaction portion. This is done by finding from the early pressurization rate an effective value of the product of "melt interfacial area density" times the melt emissivity (i.e. $6E_f/d_f$) and using it to estimate radiative power for all subse-

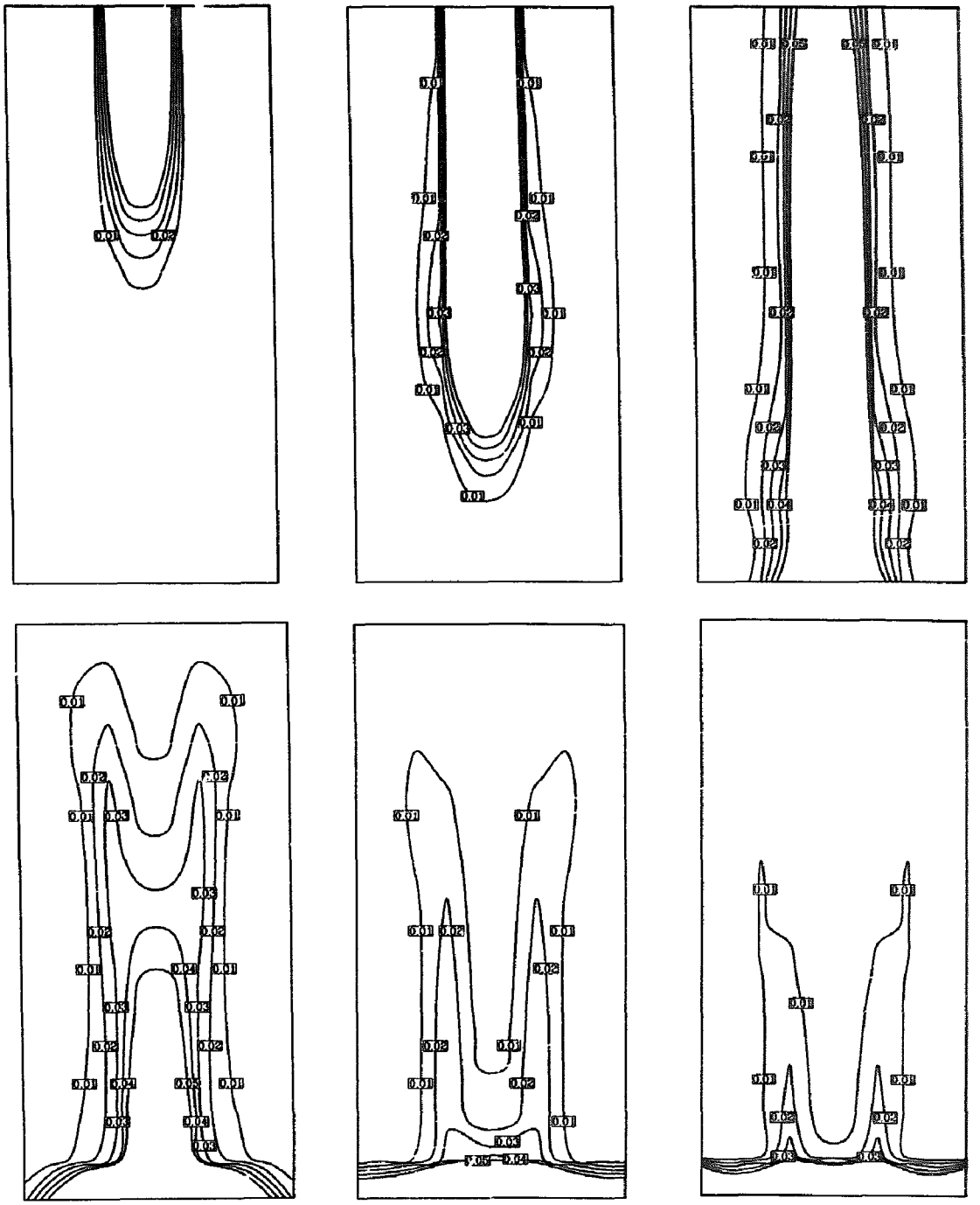

Fig. 18. Melt Volume fraction distributions at selected times in the simulation of the FARO scoping test. Times (from the initial melt release) are 0.53 s, 0.63 s, 0.73 s, 0.83 s, 0.93 s and 1.03 s for plots reading from left to right and top to bottom. The width of the plot is 47 cm, and the height is 97.6 cm, corresponding to the volume of the test vessel below the initial water level.

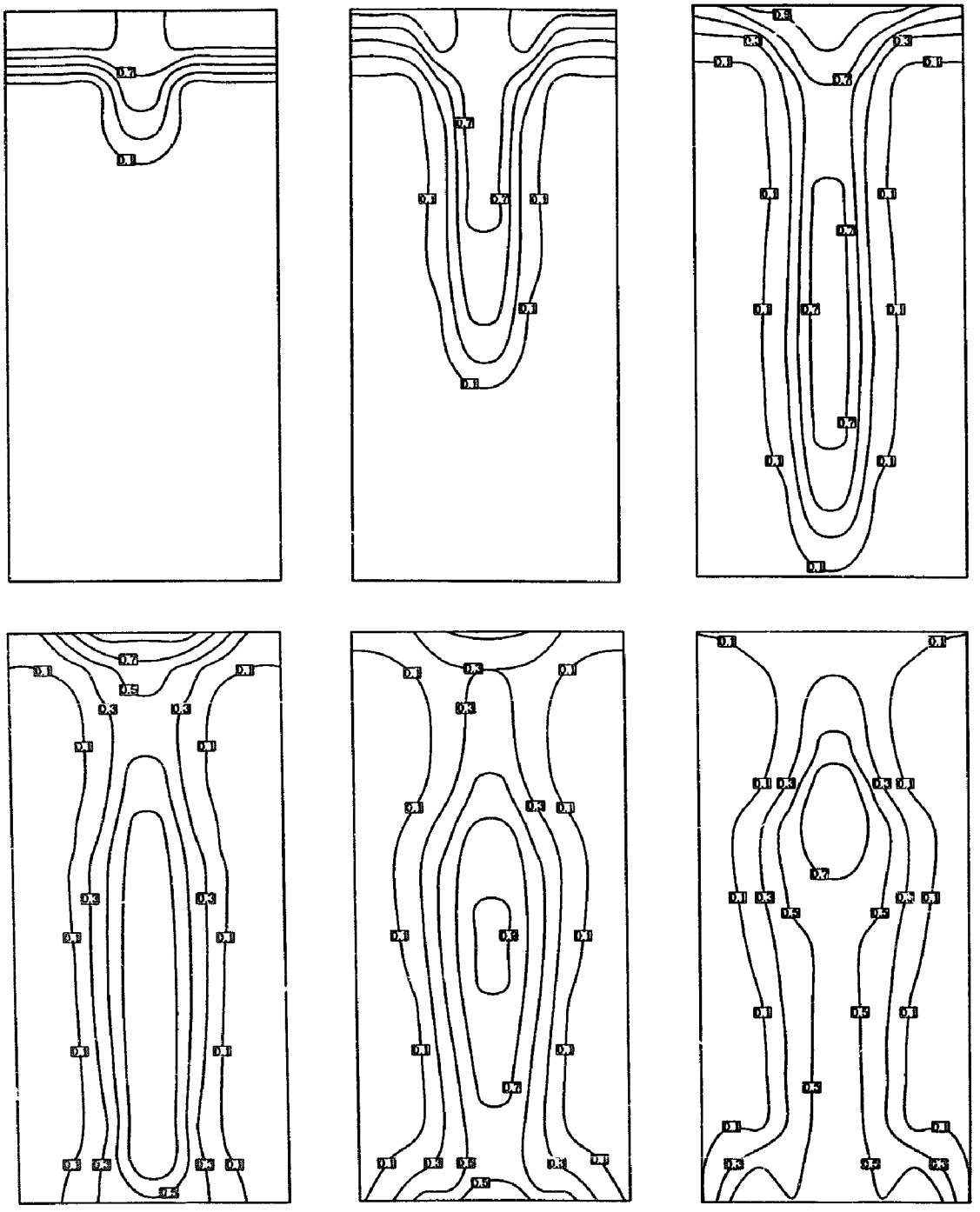

Fig. 19. Steam volume fraction distributions at selected times in the simulation of the FARO scoping test (see Fig. 18 caption for identification of time step and physical dimensions).

quent times, however, accounting for the reduction in total area as the melt "column" becomes submerged in the water pool. In actual numbers, at ~0.3 s, the pressurization rate of the gas (0.83 MPa s^{-1}) implies a uniformly applied heatup rate of 4.01 MW and a $6E_f/d_f$ value of 3.6 cm^{-1}. The latter is obtained from

$$\frac{6}{d_f} E_f \sigma T^4 \frac{m_f}{\rho_f} = \dot{Q}$$

where m_f/ρ_f is the total fuel volume, and $\dot{Q}$ is the total rate of radiative heating of the gas. Using an emissivity of 0.7, the above yields a melt particle size of 1.2 cm, which is certainly a reasonable degree of breakup of the ensuing melt jet under the conditions of this experiment (crusts were observed within the nozzle as well as in the melt catcher).

Finally, regarding further melt breakup within the interaction zone, by consideration of Weber number criteria, and with a melt-entry (the pool) velocity of 4 m s^{-1}, we estimate an initial breakup to mm-size particles. However, as the liquid pool is penetrated and set in downward motion (see earlier discussion on MAGICO) by the high velocity "swarm" of particles, the relative velocities decrease, and the continuous phase density decreases, which would tend to moderate this extensive initial breakup. For the calculation reported here, we chose a value of 0.5 cm. It happened that this first choice gave a good (compared to the experiment) timing for traversing the 0.87 m depth of the pool and also a good agreement with the interaction features of the calculation (pressurization). The fragmented debris found in the melt catcher was reported to have a mean particle size of 4.5 mm; however, from the photographs and the discussion, it appears that this fragmented debris represents only a relatively small fraction of the total melt; much of it collected as a "conglomerate in contact with the bottom plate. This part was certainly still molten when it contacted the plate" (Magallon, 1992). Thus, the chosen size of 0.5 cm may not be unreasonable, and as seen below, the degree of quenching obtained in the calculation with such a particle size appears to be consistent with a large fraction of the mass arriving in still molten form at the catcher.

As a final point in this discussion, we need to mention that we do not agree with the discussion in the quick-look report (Wider, 1992) about the role of argon gas (used initially as a cover gas) and about the transient phenomena associated with the small expansion of the gas volume due to the opening of valve SO2. First, the argon atom is considerably heavier than the steam molecule, and there is no way for it to stratify under the conditions of the experiment as claimed. Second, starting from 0.4 MPa pressure at 80 °C, as stated, the argon partial pressure at 265 °C should be ~0.7 MPa, and with the partial pressure of steam (at 265 °C) should add up to 5.77 MPa, which is significantly higher than the measured value of 5.33 MPa. This is not surprising given the method and power of heating and likely heat losses. Third, after opening the valve, the system pressure decay was arrested at ~5.07 MPa by water flashing to steam, as it should; however, because of the argon gas pressure, the pressure could not increase significantly above this value by flashing, as claimed in the quick-look report. (Free surface vaporization could provide some additional steam; however, it would be too slow to make a difference at the time frame (< 1 s) of interest.) We conclude that the pressurization above 5.07 MPa is solely due to radiative heating, and steaming, of course, after melt–water contact. That is, the situation is quite straightforward, and the method of simulation described above is quite appropriate.

The results of the calculations are discussed next. Starting from the "bottom-line" results in Figs. 11 and 12, we see the comparisons with the data on the pressurization transient and the pressurization rate, respectively. The agreement is remarkably good. In Fig. 13, we see the water subcooling (at a position away from the interaction zone) building up rapidly as a result of the pressurization, a feedback quite important to the phase change processes within the mixing-zone. The temperature rises quickly to saturation as the fuel penetrates deeper into the pool. The pressurization mechanism, initially due to radiative heating of the gas space, gradually reverts to the supply of superheated steam from the interaction zone. This can be seen from Fig. 14 showing the

"sinking" history of the melt in the water pool, Fig. 15 showing the change in radiative heating of a typical volume element in the gas space as a result of this "sinking" of the melt, and Fig. 16 showing the temperature transient of a typical cell in the gas space. This temperature transient is very consistent with that measured experimentally. In Fig. 17, we see the buildup of fuel volume fractions at the bottom cell; the timing is in excellent agreement with the data. The level swell reported for this experiment is 13 cm, which is also in remarkable agreement with the calculated value of 12 cm. Finally, a sampling of the evolution of calculated fuel and volume fraction distributions at different times during the transient are shown in Figs. 18 and 19, respectively. Because of the large aspect ratio of the full facility, the distributions below the initial water level are only shown in these figures.

To conclude, these are very promising comparisons for a first calculation, and they indicate rich possibilities for further more detailed calculations and interpretations. In particular, we hope to examine the role of different degrees of breakup during the interaction with water, and hence to be able to backup more conclusively what actually took place in the experiment. This type of information would be most helpful in carrying out premixing calculations for reactor conditions.

7. Conclusions

The water depletion phenomenon in premixing transients has been simulated in MAGICO, measured by FLUTE and by quantitative X-ray radiography, and predicted by PM-ALPHA. Moreover, PM-ALPHA seems to also predict some key multidimensional internal features of the flow field and thermal interaction regimes that appear to be consistent with what is observed in MAGICO. These latter results suggest additional experimental work in MAGICO for further insights into the detailed phenomena. By design, MAGICO allows no free parameters in analytical model predictions and is well-suited for unambiguous testing of the three-fluid and phase-change aspects of the formulation. At the other extreme, the FARO experiment with prototypic high temperature materials, high pressures, and unknown melt particulation during the transient provides some interesting challenges to analytical interpretations. We show, by means of comparison with the results of the scoping test, that PM-ALPHA can be fruitfully applied in a rather straightforward manner. Perhaps more importantly, these interpretations offer significant new insights on the effect of subcooling, as a feedback mechanism in closed (or constrained) systems, on the extent of vapor production and resulting voiding pattern. Future work will carry further these results to understanding the breakup and associated thermal interaction behavior.

Acknowledgments

This work was supported by the US Nuclear Regulatory Commission under Contract Number 04-89-084.

Appendix A: Formulation of the PM-ALPHA model

A1. Conservation equations

There are three separate phases: namely, coolant vapor, coolant liquid, and fuel (melt) drops. They will be referred to as gas, liquid, and fuel, respectively. Each phase is represented by one flow field with its own local concentration and temperature. Thus, we have three continuity equations, three momentum equations, and three energy equations. In the usual manner, the fields are allowed to exchange energy and momentum with each other, but only the steam and water fields are allowed to exchange mass. With the definition of the macroscopic density of phase i,

$$\rho_i' = \theta_i \rho_i \quad \text{for } i = \text{g, l and f} \tag{A1}$$

and the compatibility condition,

$$\theta_g + \theta_l + \theta_f = 1 \tag{A2}$$

these equations can be interpreted rather directly (Ishii, 1975).

Continuity equations

Gas:

$$\frac{\partial \rho'_g}{\partial t} + \nabla \cdot (\rho'_g u_g) = J \tag{A3}$$

Liquid:

$$\frac{\partial \rho'_l}{\partial t} + \nabla \cdot (\rho'_l u_l) = -J \tag{A4}$$

Fuel

$$\frac{\partial \rho'_f}{\partial t} + \nabla \cdot (\rho'_f u_f) = 0 \tag{A5}$$

Momentum equations

Gas:

$$\frac{\partial}{\partial t}(\rho'_g u_g) + \nabla \cdot (\rho'_g u_g u_g) = -\theta_g \nabla p - F_{gl}(u_g - u_l) - F_{gf}(u_g - u_f) + J(H[J]u_l + H[-J]u_g) + \rho'_g g \tag{A6}$$

Liquid:

$$\frac{\partial}{\partial t}(\rho'_l u_l) + \nabla \cdot (\rho'_l u_l u_l) = -\theta_l \nabla p - F_{gl}(u_g - u_l) - F_{lf}(u_l - u_f) - J(H[J]u_l + H[-J]u_g) + \rho'_l g \tag{A7}$$

Fuel:

$$\frac{\partial}{\partial t}(\rho'_f u_f) + \nabla \cdot (\rho'_f u_f u_f) = -\theta_f \nabla p + F_{gf}(u_g - u_f) + F_{lf}(u_l - u_f) + \rho'_f g \tag{A8}$$

Energy equations

Gas:

$$\frac{\partial}{\partial t}(\rho'_g I_g) + \nabla \cdot (\rho'_g I_g u_g) = -p\left[\frac{\partial \theta_g}{\partial t} + \nabla \cdot (\theta_g u_g)\right] + J(H[J]h_l + H[-J]h_g) - R_{gs}(T_g - T_s) + \dot{Q}_{fg} \tag{A9}$$

Liquid:

$$\frac{\partial}{\partial t}(\rho'_l I_l) + \nabla \cdot (\rho'_l I_l u_l) = -p\left[\frac{\partial \theta_l}{\partial t} + \nabla \cdot (\theta_l u_l)\right] - J(H[J]h_l + H[-J]h_g) - R_{ls}(T_l - T_s) + \dot{Q}_{fl} \tag{A10}$$

Fuel:

$$\frac{\partial}{\partial t}(\rho'_f I_f) + \nabla \cdot (\rho'_f I_f u_f) = -\dot{Q}_{fg} - \dot{Q}_{fl} \tag{A11}$$

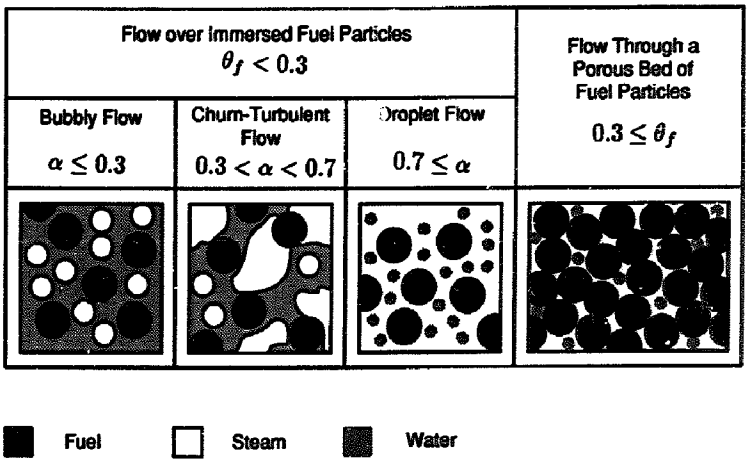

Fig. A1. Schematic diagram of flow regimes considered in characterizing interface transfers.

In the above equations $H[J]$ is the Heavyside step function that becomes unity for positive values of the argument and zero otherwise, and J is given by

$$J = \frac{1}{h_g - h_l}[R_{gs}(T_g - T_s) + R_{ls}(T_l - T_s)]$$

It should be pointed out that diffusive transport *within* each field (shear stresses and conduction) has been ignored in the above formulation. Indeed, resolution of the shear layers would impose quite more extensive demands on the computation in both nodalization and the physics of turbulence processes responsible for such transport. Although this is certainly an area for further improvement, we doubt that it will materially change the results for the particular process quantified here.

A2. The exchange laws

The interfacial exchanges of mass, momentum and energy are clearly regime dependent, and uncertainties remain even for two-phase flows. For now, our approach aims to incorporate first-order physics that account for the major flow and heat transfer regimes as identified by simple criteria of fuel volume fraction, θ_f, and gas void fraction, α, i.e. $\alpha = \theta_g/(\theta_g + \theta_l)$. The flow regimes are shown in Fig. A1. For $\theta_f < 0.3$ we consider the fuel particles immersed in a two-phase gas–liquid flow, whose own flow regimes are defined by the value of the void fraction: $\alpha \leqslant 0.3$ (bubbly), $0.3 < \alpha < 0.7$ (churn-turbulent), and $\alpha \geqslant 0.7$ (droplet). For $\theta_f \geqslant 0.3$, as the fuel particles are densely packed, we considered a flow of gas and liquid through a porous bed of fuel particles.

We use the exchange laws available for two-phase systems after making suitable modifications to account for, as a first approximation, the effect of a third phase. In calculating interfacial momentum exchange, one needs to know the projected area concentration of the dispersed phase. Also, in calculating interfacial heat exchange, one needs to know the interfacial area concentration. In a two-phase system, these area concentrations can be estimated from the length scale and the volume fraction of the dispersed phase. However, the presence of a third phase reduces the area concentration as the third phase must also share the same area. Therefore, we modify the area concentration, by a factor, ϕ_{ij}; ϕ_{ij} representing the effect of the phase k on the area concentration of phase i for its interaction with phase j. This is calculated from the respective volume fractions as

$$\phi_{ij} = \frac{\theta_j}{\theta_j + \theta_k} \tag{A12}$$

Note that with this definition ϕ_{ij} lies between 0 and 1.

A2.1. Interfacial momentum coupling

The interfacial momentum coupling is primarily due to drag. For the bubbly flow regime ($\alpha < 0.3$) we have also included the added mass effect as given by Wallis (1969)

$$F_a = \frac{\theta_g}{3 - \theta_g}\rho_l \frac{1}{|\boldsymbol{u}_g - \boldsymbol{u}_l|}\left|\frac{\partial}{\partial t}(\boldsymbol{u}_g - \boldsymbol{u}_l)\right| \tag{A13}$$

For $\theta_f < 0.3$ the drag force is based on Ishii and Zuber (1979). Specifically,

$$F_{ij} = \frac{3}{4}\theta_i \phi_{ij} \rho_j \frac{C_{Dij}}{l_i}|\boldsymbol{u}_i - \boldsymbol{u}_j| \tag{A14}$$

where suffices i and j refer to dispersed and continuous phases, respectively. The drag coefficient for churn flow ($0.3 < \alpha < 0.7$) is defined by

$$i = g,\ j = l,\ C_{Dij} = \frac{8}{3}(1 - \alpha)^2$$

and

$$l_i = 4\left\{\frac{g\Delta\rho}{\gamma}\right\}^{-1/2} \tag{A15}$$

For dispersed flow we have

$$C_{Dij} = \frac{2}{3} l_i \left\{\frac{g\Delta\rho}{\gamma}\right\}^{1/2}\left\{\frac{1 + 17.67(f(\alpha_i))^{6/7}}{18.67 f(\alpha_i)}\right\}^2 \tag{A16}$$

where

$$i = g,\ j = l,\ \alpha \leqslant 0.3 \quad f(\alpha_i) = (1 - \alpha)^{1.5} \tag{A17}$$

$$i = l,\ j = g,\ \alpha > 0.7 \quad f(\alpha_i) = \alpha^3 \tag{A18}$$

$$i = f,\ j = g, l, \quad f(\alpha_i) = (1 - \theta_f)^{1.5} \tag{A19}$$

and l_i is obtained from

$$\frac{\rho_j |u_l - u_g|^2 l_i}{\gamma} = We_{cr} \begin{cases} 8 & \text{for } i = g \\ 12 & \text{for } i = l \end{cases} \quad \text{(A20)}$$

For the "dense fuel regime" ($\theta_f > 0.3$) we use laminar and turbulent permeabilities (Sissom, 1972).

$$F_{if} = F'_{if} + F^t_{if}, \quad i = g, l \quad \text{(A21)}$$

where

$$F'_{if} = \begin{cases} 150 \dfrac{\theta_i \theta_f^2}{(1-\theta_f)^3} \dfrac{\mu_i}{l_f^2}, & \text{for } Re'_i < 1000 \\ 0, & \text{for } Re'_i \geq 1000 \end{cases} \quad \text{(A22)}$$

and

$$F^t_{if} = \begin{cases} 1.75 \dfrac{\theta_i \theta_f}{(1-\theta_f)^3} \dfrac{\rho'_i |u_i - u_f|}{l_f}, & \text{for } Re'_i > 10 \\ 0, & \text{for } Re'_i \leq 10, \end{cases} \quad \text{(A23)}$$

$$Re'_i = \theta_f \frac{\rho'_i l_f |u_i - u_f|}{\mu_i} \quad \text{(A24)}$$

It is noted, however, that this regime is of very limited relevance to computations of practical interest.

A2.2. Interfacial heat transfer and phase change

The distinction of the fuel-to-coolant heat transfer mechanisms is made again on the basis of the flow regimes. The key distinction is whether or not there is sufficient water in the coolant phase to completely engulf the fuel particles, thus a gas void fraction criterion is used.

For $\alpha < 0.7$, heat transfer to liquid is estimated by superposition of radiation and film boiling heat fluxes. That is,

$$\dot{Q}_{fl} = n_f (h_r + h_c) \pi l_f^2 \phi_{fl} (T_f - T_l) \quad \text{(A25)}$$

where

$$n_f = \frac{6\theta_f}{\pi l_f^3} \quad \text{(A26)}$$

$$h_r = \sigma E_f \frac{T_f^4 - T_l^4}{T_f - T_l} \quad \text{(A27)}$$

and (Witte, 1968; Liu, 1992)

$$h_c = 2.98 \left\{ \frac{\rho_g k_g [h_{fg} + 0.68 c_{pg} (T_f - T_l)]}{l_f (T_f - T_l)} |u_f - u_l| \right\}^{1/2} \quad \text{(A28)}$$

The emissivity value $E_f = 0.7$ is selected for the calculations of typical interest. Heat transfer from fuel to gas in this regime need not be accounted for separately.

For $\alpha > 0.7$, we assume a vapor-continuous regime in which heat is transferred to liquid drops by irradiation and to the gas by convection. The gas is allowed to superheat and convect heat to the liquid drops which boil at saturation. Thus

$$\dot{Q}_{fl} = \min(n_l \pi l_l^2, n_f \pi l_f^2) \sigma E_f E_l (T_f^4 - T_l^4) \quad \text{(A29)}$$

and

$$\dot{Q}_{fg} = n_f \phi_{fg} \pi l_f^2 h'_c (T_f - T_g) \quad \text{(A30)}$$

where $n_l = 6\theta_l / \pi l_l^3$ and h'_c is given by Bird et al. (1960): for $\theta_f < 0.3$

$$h'_c = \frac{k_g}{l_f} \{2 + 0.6\, Re_g^{1/2}\, Pr_g^{1/3}\} \quad \text{(A31)}$$

where

$$Re_g = \frac{\rho_g |u_g - u_f| l_f}{\mu_g} \quad \text{(A32)}$$

and for $\theta_f \geq 0.3$,

$$h'_c = 0.91 c_{pf} \rho'_g |u_g - u_f|\, Re''^{-0.51}_g\, Pr_g^{-2/3} \quad \text{for } Re''_g \leq 50 \quad \text{(A33)}$$

$$h'_c = 0.61 c_{pf} \rho'_g |u_g - u_f|\, Re''^{-0.41}_g\, Pr_g^{-2/3} \quad \text{for } Re''_g > 50 \quad \text{(A34)}$$

where

$$Re''_g = \frac{\rho'_g l_f |u_g - u_f|}{6\theta_f \mu_g} \quad \text{(A35)}$$

The factor E_l in Eq. (29) was introduced to empirically degrade the radiation heat transfer to liquid by the portion that could not be absorbed. For reactor calculations we typically use $E_l = 0.3$ to conservatively bias the predictions.

Similarly, for vapor-to-liquid heat transfer we have, for $\alpha < 0.7$ with vapor as the dispersed phase,

$$R_{ls} = c_l n \phi_{gl} \pi l_g^2 \frac{k_l}{g_g} \{2 + 0.6\, Re^{1/2}\, Pr_l^{1/3}\} \quad \text{(A36)}$$

$$R_{gs} = 2 n_g \phi_{gl} \pi l_g^2 \frac{k_g}{l_g}$$

while for $\alpha > 0.7$, with liquid (drops) as the dispersed phase

$$R_{gs} = n_l \phi_{lg} \pi l_l^2 \frac{k_g}{l_l} \{2 + 0.6\,\mathrm{Re}^{1/2}\,\mathrm{Pr}_g^{1/3}\} \qquad \text{(A37)}$$

$$R_{ls} = 2 c_l \eta_l \phi_{lg} \pi l_l^2 \frac{k_l}{l_l}$$

In the above the coefficient c_l was introduced as a way to control the liquid superheat in cases where these simplified formulations for heat transfer coefficients are not deemed adequate.

Appendix B: Independent verification of the FLUTE measurements

The reason for creating the FLUTE is that our efforts in using absorbing radiation to image the whole mixing zone during the design phase of MAGICO did not yield promising results. The working concept in this effort was to make use of two different γ- and X-ray energies and the differences in attenuation between the water and the material of the balls so as to simultaneously measure both. Although in principle this approach is fine, in practice, it results in a stiff system of equations that yield large error amplification in the solution, and thus it was abandoned.

We returned to it recently after the completion of the first phase of the experimental program in MAGICO that made use of FLUTE. The reapproach appeared hopeful, basically because actual experience with MAGICO indicated that the particle volume fractions in the mixing zone are in the 2–3% range, thus creating the possibility of "seeing" through limited (sporadic) areas of this zone without ball interference. Numerical experiments attempting to recreate realization of the particle cloud and the optical paths through it revealed that this was indeed the case. These experiments also provided guidance on how to optimize the orientation of the X-ray shot and the source-to-object distance, taking advantage of the hole pattern in the dumper plate.

Fig. B1. Print of the X-ray film taken in run no. 1005.

In actual implementation, we used a flash of "soft" X-rays timed at the desired instant within the premixing transient in MAGICO. The image is recorded on a 13 × 18 cm film positioned to cover the region of interest in the mixing zone. By changing the timing of the flash and the film position, we can map out a premixing transient in any temporal and spatial detail desired; this is possible because of the excellent reproducibility of the MAGICO runs, as already demonstrated by the FLUTE measurements and the high-speed movies. We have limited our goal here to the independent check of the FLUTE results, and only a few runs are adequate for this purpose. In the process of developing the quantitative aspects of this technique, we have made quite a few runs that successively appeared more and more promising. A great deal of the success depends on establishing adequate safeguards and procedures to ensure that the image obtained can be directly related to a calibration image obtained with a stepwise variation of void in the optical path. In addition, we confirmed that the effect of X-ray scattering from the steel balls (they are not present, clearly, in the calibration shot) is negligible. At this time, the technique is well developed, and we have one run in the MAGICO series (the 1000-series) to discuss here. Rather than carry out the many special FLUTE runs needed to cover the information on the X rays, our approach is to use PM-ALPHA as the means of comparison; the PM-ALPHA interpretations are the ultimate purpose in any case.

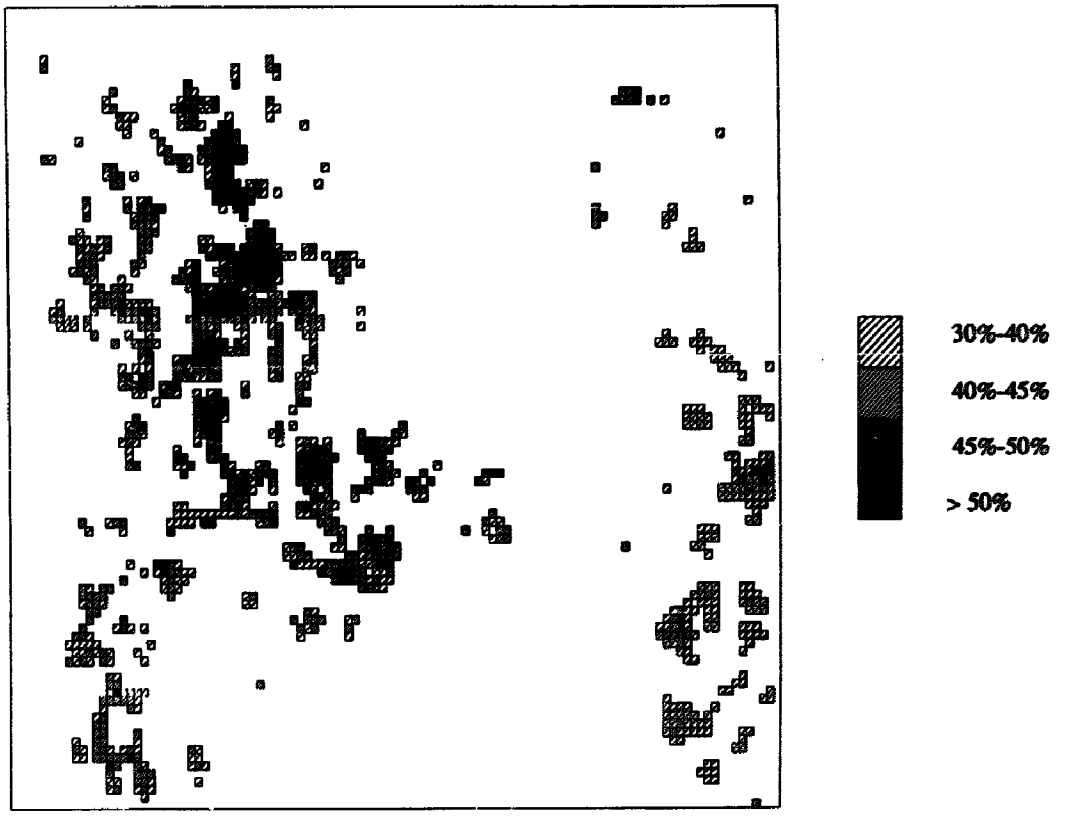

Fig. B2. Void fraction distribution obtained from X-ray analysis of run no. 1005. The region covered is $-1.5 < r < 5.5$ cm and $19 < z < 25$ cm.

This MAGICO test, no. 1005, was run with the 2.4-mm steel balls at 600 °C poured into a 25-cm deep pool of saturated water from a height of 21 cm. The X-ray shot was timed at 0.52 s after initiation of the pour, which corresponds to just about when the particle front hits the pool bottom. The X-ray image obtained is shown in Fig. B1. It is noteworthy that individual balls are recognizable, even when they partly overlap, and we believe with a pattern recognition technique, we will have, from such shots, the particle number densities as well. Also in this figure, small areas where balls are completely absent are clearly distinguishable, and it is in these areas that with the application of the water/void calibration curve we can obtain the chordal-average void fractions.

The "reading" and analysis of these films was done on 6 × 6 cm film segments in order to obtain the high resolution required; this gave a pixel size of 0.12 mm. These readings were analyzed in groups of 20 pixels. For each such group, an average value of void (and hence of void fraction) was obtained by using the calibration curve and a criterion excluding readings indicating the presence of spheres. Moreover, to ensure that readings too close to the sphere boundaries were excluded, we used as an additional criterion that the fraction of unaffected readings within a group was above some value; otherwise, the space associated with the particular group of (20) pixels was taken to be affected by the presence of steel. The data analysis was repeated with f values of this fraction

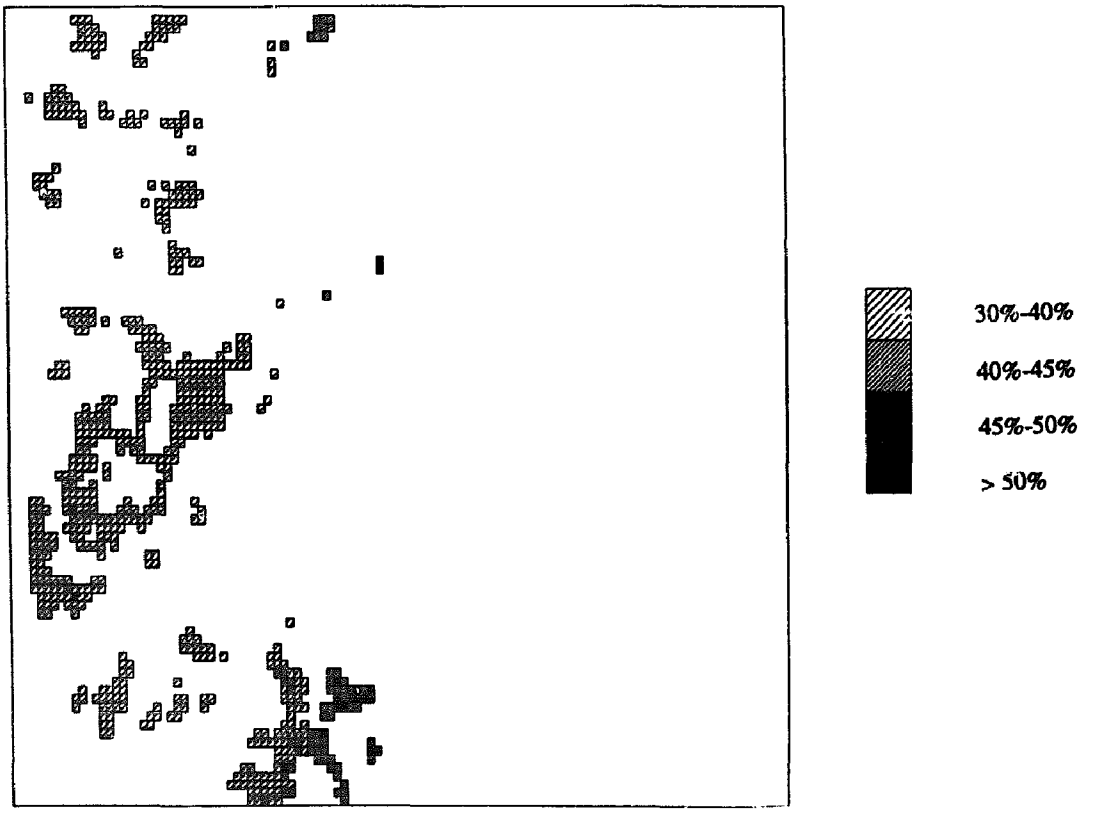

Fig. B3. Void fraction distribution obtained from X-ray analysis of run no. 1005. The region covered is $5.5 < r < 11.5$ cm and $19 < z < 25$ cm.

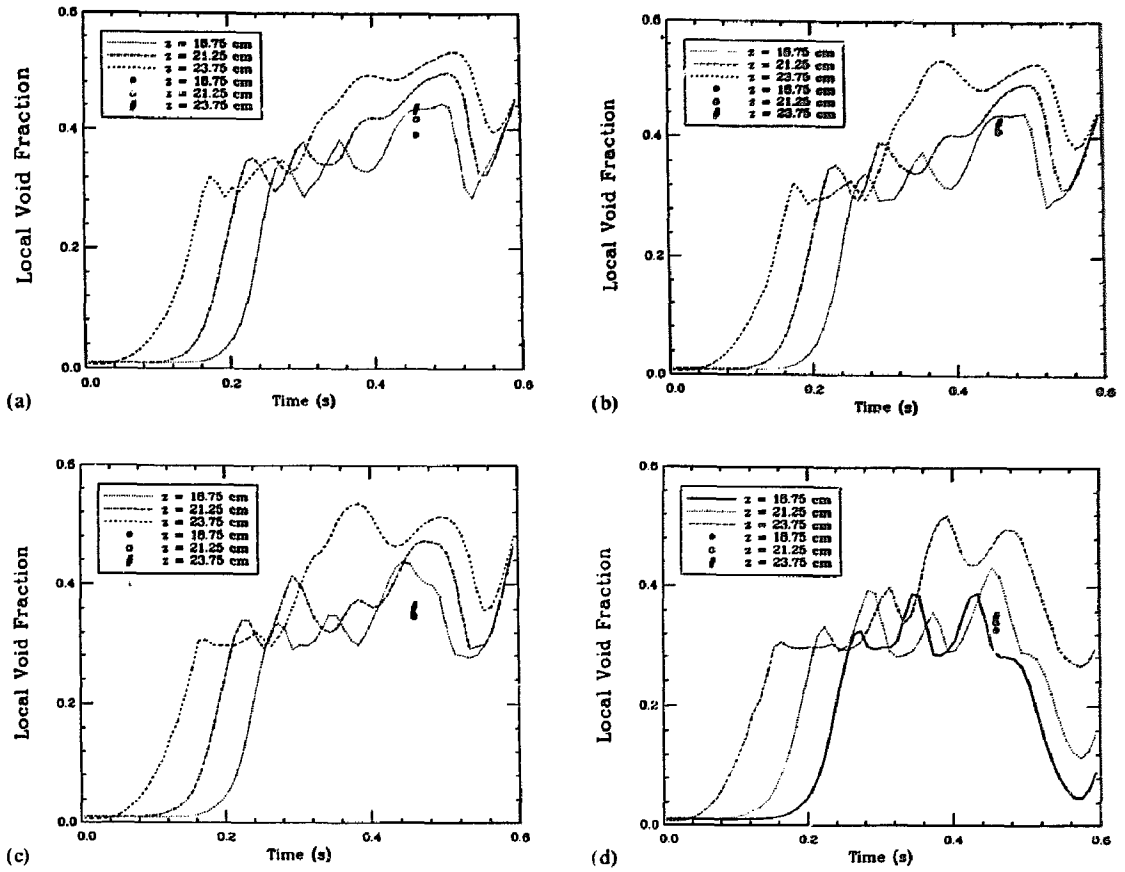

Fig. B4. Comparison between prediction and X-ray measurement for run no. 1005 for cell centered at (a) $r =$ ' cm and three different heights; (b) $r = 3$ cm and three different heights; (c) $r = 5$ cm and three different heights; (d) $r = 7$ cm and three different heights.

set to 25, 50, and 75%, with very consistent results, indicating absence of the boundary-type influence being addressed by this operation.

The results from film segments covering the region $19 < z < 25$ cm (i.e. a 6-cm slice of the pool top; z is measured from the pool bottom) over two radial segments, $-1.5 < r - 5.5$ cm and $5.5 < r < 11.5$ cm presented here. Spatial void fraction maps (using the 50% criteria discussed above) are shown in Figs. B2 and B3 for the above two radial regions, respectively. The blank spaces in these maps indicate regions at ball interference. Immediately, we can notice that these results indicate void fractions in the general range measured by FLUTE (Angelini, 1992). In a more detailed examination, we have plotted these results against PM-ALPHA predictions for four different radial computational cells (at $r = 1$, 3, 5, and 7 cm) at three axial positions ($z = 18.75$, 21.25, and 23.75 cm), as shown in Fig. B4. In these figures, the PM-ALPHA results were obtained by an appropriate chordal-average equivalent to projecting the cylindrically symmetric void fraction distribution, as effected by the X-ray on the film. The X-ray results were obtained from the spatial maps by averaging all measured values within the cell being considered. The agreement is quite remarkable in all cases. It is also interesting to note that

the "water flux reversal" phenomenon discussed in Section 4 is quite evident in Fig. B4(d); the insurge of water causes a precipitous drop of void fraction at the outer edges of the mixing zone. The X-ray happened to be taken just prior to this time, but it is clear now how to best time the X-ray shot in the next run.

Appendix C: Nomenclature

C_D drag coefficient
c_l control coefficient
c_p specific heat at constant pressure
E_f emissivity of fuel particles
E_l absorptivity of water droplets
F factor for interfacial momentum exchange
g acceleration of gravity
H Heaviside step function
h heat transfer coefficient; specific enthalpy
h_{fg} enthalpy of evaporation
I specific internal energy
J phase change rate per unit volume
k thermal conductivity
l length scale
n number of particles (or drops) per unit volume
Pr Prandtl number
p pressure
$\dot{Q}$ rate of heat transfer per unit volume
R heat transfer coefficient between the phase (liquid or vapor) and interface
Re Reynolds number
T temperature
t time
u velocity vector
We_{cr} critical Weber number for bubble/drop breakup

Greek letters

α void fraction of vapor (per unit volume of coolant)
γ surface tension between vapor and liquid; specific heat ratio
θ volume fraction (per unit volume of total mixture)
μ viscosity
ρ microscopic density
ρ' macroscopic density
σ Stefan–Boltzmann coefficient
ϕ_{ij} area concentration factor, defined in Eq. (A12)

Subscripts

a added-mass effect
c convection
f fuel
g gas (steam)
l liquid water
r radiation
s saturation

Superscripts

l laminar flow
t turbulent flow

References

M.A. Abolfadl and T.G. Theofanous, An assessment of steam-explosion-induced containment failure. Part II: premixing limits, Nucl. Sci. Eng. 97 (1987) 282.

W.H. Amarasooriya and T.G. Theofanous, Premixing of steam explosions: a three-fluid model, Nucl. Eng. Des. 126 (1991) 23–39.

S. Angelini, E. Takara, W.W. Yuen and T.G. Theofanous, Multiphase transients in the premixing of steam explosions, Proc. NURETH-5, Salt Lake City, UT, 1992, Vol. II, 1992, pp. 471–478.

S.G. Bankoff and S.H. Han, An unsteady one dimensional two-fluid model for fuel-coolant mixing in an LWR melt-down accident, Proc. US/Japan Sem. on Two-Phase Dynamics, Lake Placid, New York, 1984.

R.B. Bird, W.E. Stewart and E.N. Lightfoot, Transport Phenomena, Wiley, New York, 1960.

M.K. Denham, A.P. Tyler and D.F. Fletcher, Experiments on the mixing of molten uranium dioxide with water and initial comparisons with CHYMES code calculations, Proc. NURETH-5, Salt Lake City, UT, 1992.

D.F. Fletcher and A. Thyagaraja, The CHYMES coarse mixing model, Prog. Nucl. Energy 26 (1991) 31–61.

D.F. Fletcher, A comparison of coarse mixing predictions obtained from the CHYMES and PM-ALPHA models, Nucl. Eng. Des. 135 (1992) 419–425.

R.E. Henry and H. K. Fauske, Required initial conditions for energetic steam explosions, Fuel-Coolant Interactions, HTD-V19, American Society of Mechanical Engineers, 1981.

M. Ishii, Thermo-Fluid Dynamic Theory of Two-Phase Flow, Eyrolles, 1975.

M. Ishii and N. Zuber, Drag coefficient and relative velocity in bubbly, droplet or particulate flows, AIChE J. 5 (1979) 843.

C. Liu, T.G. Theofanous and W. Yuen, Film boiling from spheres in single- and two-phase flow, ANS Proc. National Heat Transfer Conf., San Diego, CA, Vol. 6, 1992, pp. 211–218.

D. Magallon et al., FARO LWR programme, scoping test data report, Technical Note No I.92.135, Institute for Safety Technology, 1992.

D. Magallon and H. Hohmann, High pressure corium melt quenching tests in FARO, CSNI Specialists Meet. on Fuel–Coolant Interactions, Santa Barbara, CA, 1993.

L.E. Sissom and D.R. Pitts, Elements of Transport Phenomena, McGraw-Hill, New York, 1972.

Steam Explosion Review Group, A review of current understanding of the potential for containment failure arising from in-vessel steam explosions, NUREG-1116, US Nuclear Regulatory Commission, 1985.

T.G. Theofanous, B. Najafi and E. Rumble, An assessment of steam-explosion-induced containment failure. Part I: probabilistic aspects, Nucl. Sci. Eng. 97 (1987) 259–281.

T.G. Theofanous, S. Angelini, R. Buckles and W.W. Yuen, On the prediction of steam explosions energetics, Proc. 19th Water Reactor Safety Information Meet., 1991.

T.G. Theofanous, W.W. Yuen, S. Angelini, X. Chen, W.H. Amarasooriya, S. Medhekar and H. Yan, Steam explosions: fundamentals and energetic behavior, NUREG/CR-5960, US Nuclear Regulatory Commission, 1992.

T.G. Theofanous, W.W. Yuen and B.W. Sheron, The probability of alpha-mode containment failure updated, CSNI Specialists Meet. on Fuel-Coolant Interactions, Santa Barbara, CA, 1993.

G.B. Wallis, One-dimensional Two-phase Flow; McGraw-Hill, New York, 1969.

H.U. Wider et al., The FARO/LWR experimental programme, IRC Technical Note No. I.92.139, 1992.

L.C. Witte, Ind. Eng. Chem. Fundam. 7 (1968) 517.

W.W. Yuen and T.G. Theofanous, The fundamental mechanisms and structure of thermal detonations, CSNI Specialists Meet. on Fuel-Coolant Interactions, Santa Barbara, CA, 1993.